PHYSICAL REVIEW D **90,** 104004 (2014)

Remnant mass, spin, and recoil from spin aligned black-hole binaries

James Healy, Carlos O. Lousto, and Yosef Zlochower
Center for Computational Relativity and Gravitation, School of Mathematical Sciences, Rochester Institute of Technology, 78 Lomb Memorial Drive, Rochester, New York 14623, USA
(Received 27 June 2014; published 6 November 2014)

We perform a set of 36 nonprecessing black-hole binary simulations with spins either aligned or counteraligned with the orbital angular momentum in order to model the final mass, spin, and recoil of the merged black hole as a function of the individual black-hole spin magnitudes and the mass ratio of the progenitors. We find that the maximum recoil for these configurations is $V_{\rm max} = 526 \pm 23$ km s^{-1}, which occurs when the progenitor spins are maximal, the mass ratio is $q_{\rm max} = m_1/m_2 = 0.623 \pm 0.038$, the smaller black-hole spin is aligned with the orbital angular momentum, and the larger black-hole spin is counteraligned ($\alpha_1 = -\alpha_2 = 1$). This maximum recoil is about 80 km s^{-1} larger than previous estimates, but most importantly, because the maximum occurs for smaller mass ratios, the probability for a merging binary to recoil faster than 400 km s^{-1} can be as large as 17%, while the probability for recoils faster than 250 km s^{-1} can be as large as 45% when the spins are aligned or counteraligned by accretion. We provide explicit phenomenological formulas for the final mass, spin, and recoil as a function of the individual black-hole spins and the mass difference between the two black holes. Here we include terms up through fourth order in the initial spins and mass difference and find excellent agreement (within a few percent) with independent results available in the literature. The maximum radiated energy is $E_{\rm rad}/m \approx 11.3\%$ and final spin $\alpha_{\rm rem}^{\rm max} \approx 0.952$ for equal-mass, aligned, maximally spinning binaries.

DOI: 10.1103/PhysRevD.90.104004 PACS numbers: 04.25.dg, 04.25.Nx, 04.30.Db, 04.70.Bw

I. INTRODUCTION

The fully nonlinear simulations of merging black-hole binaries (BHBs) that were enabled by the 2005 breakthroughs in numerical relativity [1–3] revealed some unexpectedly large effects. Perhaps one of the most striking is that the merger remnant can recoil away from the center of mass by thousands of km/s for BHBs with spins at least partially in the orbital plane [4–8]. Such recoils, if common, would have major implications for structure formation and the evolution of galaxies, as well as the retention of BHs in globular clusters and the formation of intermediate mass BHs. The probability of these large recoils depends on the distribution of mass ratios and spins of the progenitor binaries. While the detailed modeling of those recoil velocities from merging BHBs as a function of the individual spins (magnitudes and directions) of the BHs and the mass ratio is well underway [8–12], the major effort required to simulate BHBs in a realistic astrophysical environment, including individual and circumbinary accretion disks, magnetohydrodynamical effects, and radiation transfer, started more recently [13–24]. Analyses of Newtonian and Post-Newtonian (PN) simulations appear to indicate that accretion dynamics will skew the spin distributions away from configurations that favor very large recoils [25–27] because these effects tend to align (or counteralign) the spins with the orbital angular momentum (see, however, the arguments about longer time scales needed for the alignment mechanism to be effective in Ref. [28]). On the other hand, recent studies of chaotic [29] and partially chaotic [30] accretion suggest that misalignment of spins can also be a common evolutionary scenario for BHBs, possibly allowing for the merger remnant to escape from large galaxies [31,32]. In addition, during the late stages of the BHB evolution, post-Newtonian resonance effects [33,34], in the "reverse mass ratio" evolution pathway scenario, tend to further align the BH spins with each other and the orbital angular momentum (or counteralign them azimuthally).

In this paper we simulate the late-inspiral and merger stages of BHBs in configurations where the spins are exactly aligned or counteraligned with the orbital angular momentum. By doing so, we are able to quantify how large the recoil can be when coherent accretion effects dominate the distribution of spin directions, thus providing a lower bound to the recoil of the BH remnant. The aligned-spin case also provides the optimal configuration for the radiation of gravitational energy and angular momentum. Here we provide a unified, higher-order phenomenological model of the remnant mass, spin, and recoil from the merger of two BHs with different masses and different spin magnitudes (either aligned or antialigned spins).

This paper is organized as follows: In Sec. II we review the current status of the modeling of the remnant recoil. In Sec. III we review the numerical techniques used for our evolutions of the BHBs and the subsequent analyses of the

progenitor and remnant properties. In Sec. IV we present the explicit form of the new phenomenological formulas for the final mass, spin, and recoil of the merger remnant. We apply these formulas to astrophysically motivated distributions of the mass ratios and spins of the progenitor binaries to obtain probabilities for a given recoil, final remnant mass, and spin. In Sec. VI we discuss the consequences of our results. In Appendix A we examine in detail a particular configuration to see the dependence of the recoil, final mass, and final spin on the initial quasicircular orbital separation, resolution, extraction radii, and maximum ℓ mode used to reconstruct the gravitational waveform. In Appendix B we compare the use of third-order versus fourth-order fitting formulas for the remnant mass, spin, and recoil.

II. MODEL OF RECOILS ON THE ORBITAL PLANE

Beginning in Ref. [4], we developed a heuristic model for the gravitational recoil of a merging binary. The model for the in-plane recoil was based on PN-inspired fitting formulas combined with the results of [35–37] (a similar model was developed independently in [38]). Here we use the PN-inspired variables

$$\begin{aligned} m &= m_1 + m_2, \\ \delta m &= \frac{m_1 - m_2}{m}, \\ \vec{S} &= \vec{S}_1 + \vec{S}_2, \\ \vec{\Delta} &= m(\vec{S}_2/m_2 - \vec{S}_1/m_1), \end{aligned}$$

where m_i is the mass of BH $i = 1, 2$ and $\vec{S}_i$ is the spin of BH i. We also use the auxiliary variables

$$\begin{aligned} \eta &= \frac{m_1 m_2}{m^2}, \\ q &= \frac{m_1}{m_2}, \\ \vec{\alpha}_i &= \vec{S}_i/m_i^2, \end{aligned}$$

where $|\vec{\alpha}_i| \leq 1$ is the dimensionless spin of BH i, and we use the convention that $m_1 \leq m_2$ and hence $q \leq 1$.

The in-plane recoil can be split (at least approximately) into two components: a part due solely to unequal masses and a part due to the out-of-plane components of the spins of the two BHs. To lowest order in the spin, the formula is given by

$$\vec{V}_{\rm recoil}(q, \vec{\alpha}_i) = v_m \hat{e}_1 + v_\perp(\cos(\xi)\hat{e}_1 + \sin(\xi)\hat{e}_2), \quad (1)$$

where

$$v_m = -A\eta^2 \delta m(1 + B\eta), \quad (2a)$$

$$v_\perp = H\eta^2\left[\frac{\Delta_\parallel}{m^2} - H_S \delta m \frac{S_\parallel}{m^2}\right]. \quad (2b)$$

Here the indices $\perp$ and $\parallel$ refer to components perpendicular to and parallel to the orbital angular momentum during the short period around merger when most of the recoil is generated, while $\hat{e}_1, \hat{e}_2$ are orthogonal unit vectors in the orbital plane, and ξ measures the angle between the "unequal mass" and "spin" contributions to the recoil velocity in the orbital plane (see Fig. 1). This formula can be extended by adding additional nonlinear terms (as we will show in this paper). The coefficients are given by $A = 1.2 \times 10^4$ km s^{-1} [35], $B = -0.93$ [35], and $H = (6.9 \pm 0.5) \times 10^3$ km s^{-1} [39]. We will study in detail how ξ depends on the configurations here (ξ was initially studied in Ref. [39], where it was found that $\xi \sim 145°$ for a range of quasicircular configurations).

A. Post-Newtonian analysis

Here we use the leading-order post-Newtonian expressions for the radiated linear momentum to get a qualitative understanding of the full numerical results. As seen in Eq. (3.31) of Ref. [40], the instantaneous radiated linear momentum due to the asymmetry in the masses of the binary is given by

$$\begin{aligned} \dot{\vec{P}}_N = -\frac{8\eta^2 \delta m}{105}\left(\frac{m}{r}\right)^4 [&(5V_T^2 - 2V_r^2 + 4m/r)V_r \hat{n} \\ &-(12V_r^2 + 50V_T^2 + 8m/r)V_T \hat{\lambda}], \end{aligned} \quad (3)$$

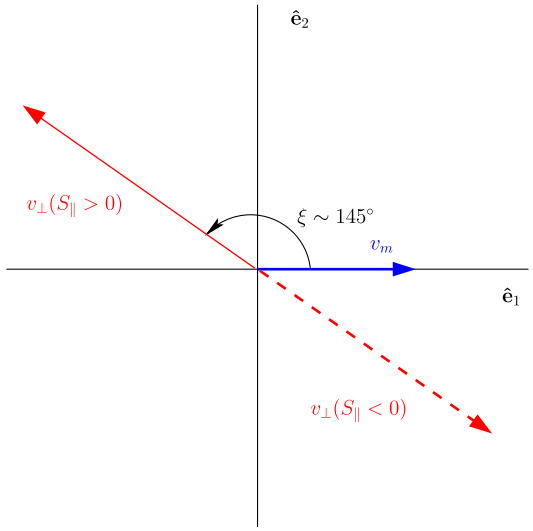

FIG. 1 (color online). A sketch showing how the angle ξ between the unequal mass contribution to the recoil and the spin-dependent contribution to the recoil depends on the sign of $S_\parallel$ (with similar behavior for the $\delta m \Delta_\parallel$-dependent term). The two components essentially add if the net spin is counteraligned with the orbital angular momentum, and they subtract if the spin is aligned with the orbital angular momentum.

and the radiated linear momentum due to the leading-order spin-orbit coupling is

$$\dot{\vec{P}}_{SO} = -\frac{8\eta^2 m}{15r^5}[4V_T V_r \hat{n} + 2(V_T^2 - V_r^2)\hat{\lambda}]\Delta_{\parallel}, \quad (4)$$

where V_T and V_r are the tangential and radial velocities, respectively. The velocity is given by $\vec{V} = V_T\hat{\lambda} + V_r\hat{n}$, where $\hat{n} = (\vec{r}_1 - \vec{r}_2)/|\vec{r}_1 - \vec{r}_2|$, $\hat{n} \times \hat{\lambda} = \hat{L}$, and $\hat{L}$ is the unit vector in the direction of the orbital angular momentum $\hat{L}$.

For a quasicircular orbit, the angle between these two components of the instantaneous radiated linear momentum is given by

$$\cos\xi^{\Delta} = \left[-1 + \frac{15625}{6728}\frac{V_r^2}{V_T^2} + \cdots\right]\mathrm{sign}(\delta m\vec{\Delta}\cdot\hat{L}), \quad (5)$$

and hence, for circular orbits, i.e., $V_r = 0$,

$$\cos\xi_c^{\Delta} = -\mathrm{sign}(\delta m\vec{\Delta}\cdot\hat{L}). \quad (6)$$

This indicates that (in our case $\delta m < 0$) the PN prediction is opposite to what we actually observe using full numerical simulations, where the two components are opposite of each other when $\vec{\Delta}$ is aligned with the orbital angular momentum (corotating orbits for our configurations), and for our counter-rotating configurations, the two components add constructively. This difference may be due to the fact that the large spin-induced recoil takes place mostly when the two black holes are merging, a regime far from the PN region of validity. It has been observed for the "hangup" [41] and superkick [42] effects that while the parameter dependence predicted by PN is in agreement with the full numerical results, the amplitude (and in this case the sign) is not correct.

For orbits dominated by the radial motion instead (i.e., $V_T \ll V_r$), the angle ξ has the form

$$\cos\xi^{\Delta} = \left[\frac{4V_T}{V_r}\frac{(rV_r^2 + 2M)}{|-rV_r^2 + 2M|} + \cdots\right]\mathrm{sign}(\delta m\vec{\Delta}\cdot\hat{L}). \quad (7)$$

Hence, in the near-headon case (i.e., $V_T \approx 0$), we have

$$\cos\xi_h^{\Delta} \approx 0, \quad (8)$$

and the two components of the recoil are perpendicular to each other, in agreement with full numerical results.

The next leading term in the spin-orbit contribution to the recoil [see Eqs. (4.7)–(4.9) of Ref. [43]] is proportional to $\delta m S_{\parallel}$. For circular orbits the angle $\cos\xi_c^S$ between the unequal mass recoil and the terms in the recoil proportional to $\delta m\vec{S}$ is given by

$$\cos\xi_c^S = -\mathrm{sign}(\vec{S}\cdot\hat{L}), \quad (9)$$

while for head-on collisions [see Eqs. (3.17) of Ref. [43]] the two components are perpendicular and

$$\cos\xi_h^S \approx 0. \quad (10)$$

In a full numerical simulation, the inspiral of two BHs is neither circular nor head-on, and hence we expect a value of ξ that lies between 90° and either 180° (corotating) or 0° (counter-rotating) (see Fig. 1). In particular, because of the hangup effect [41] we expect that aligned-spin configurations, which have tighter (i.e., more circular) orbits, have $\xi \approx 180°$, while counteraligned configurations, which inspiral much more quickly, should have $\xi \lesssim 90°$.

Based on the above analysis, we expect $\cos\xi$ to be a discontinuous function with a finite jump when $\vec{S}\cdot\vec{L}$ and $\delta m\Delta\cdot\vec{L}$ change sign. While we can model ξ as a discontinuous function, there is a way around this. Note that the magnitude of the in-plane recoil is given by

$$V^2 = (v_m + |v_\perp|\cos\xi)^2 + v_\perp^2\sin^2\xi, \quad (11)$$

where $|v_\perp|$ is the magnitude of the spin contribution to the in-plane recoil. The important thing to note is that while $\cos\xi$ is discontinuous, the recoil itself should be continuous. For this to be true, the sign change in $\cos\xi$ can only occur when $v_\perp = 0$; i.e., we expect that $|v_\perp|\cos\xi$ is continuous. We can therefore express the product $|v_\perp|\cos\xi$ as a product of two continuous functions $v_\perp$, which we will allow to be positive or negative, and $\cos\tilde{\xi}$, where $\cos\tilde{\xi}$ has a fixed sign (for historical reasons, we chose $\cos\tilde{\xi}$ to be negative) and $|\cos\tilde{\xi}| = |\cos\xi|$. Finally, the magnitude of the recoil is given by

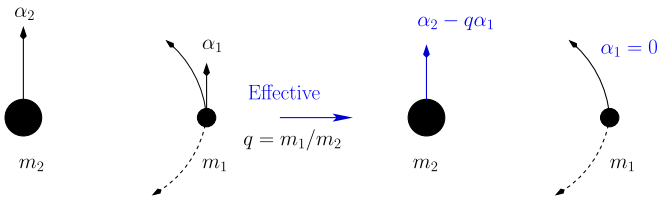

FIG. 2 (color online). The (counter)aligned spin configuration UU (DD) and its effective counterpart 0U (0D) (dashed counterorbiting).

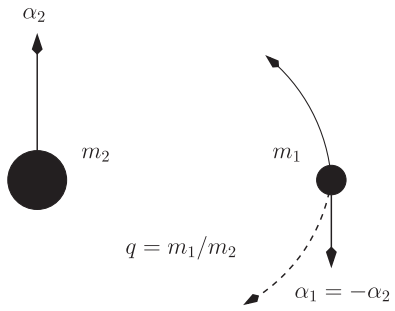

FIG. 3. The DU and UD (dashed counterorbiting) configurations.

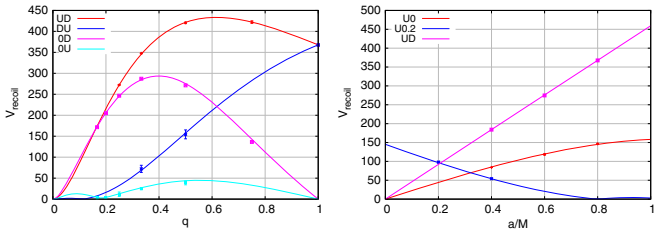

FIG. 4 (color online). The recoils for the families UD/DU/0U/0D and for the equal mass cases given in Table I.

$$V^2 = (v_m + v_\perp \cos\tilde{\xi})^2 + v_\perp^2 \sin^2\tilde{\xi}, \tag{12}$$

where $v_\perp$ can be negative and $\mathrm{sign}(v_\perp)\cos\tilde{\xi}$ is the cosine of the angle between unequal-mass and spin components of the recoil.

III. NUMERICAL SIMULATIONS

We use the TwoPunctures thorn [44] to generate initial puncture data [45] for the BHB simulations. These data are characterized by mass parameters m_p (which are not the horizon masses), as well as the momentum and spin, of each BH. We evolve these BHB data sets using the LazEv [46] implementation of the moving puncture approach [2,3] with the conformal function $W = \sqrt{\chi} = \exp(-2\phi)$ suggested by Ref. [47]. For the runs presented here, we use centered, eighth-order finite differencing in space [48] and a fourth-order Runge-Kutta time integrator. (Note that we do not upwind the advection terms.) Our code uses the Cactus/EinsteinToolkit [49–51] infrastructure. We use the Carpet [52] mesh refinement driver to provide a "moving boxes" style of mesh refinement.

We locate the apparent horizons using the AHFinderDirect code [53] and measure the horizon spin using the isolated horizon (IH) algorithm detailed in [54].

For the computation of the radiated energy and linear momentum, we use the formulas in [55] which are expressed directly in terms of the Weyl scalar ψ_4. To extract the radiation of angular momentum components, we use formulas based on "flux linkages" [56], which are explicitly written in terms of ψ_4 in [55,57].

TABLE I. Initial data parameters for the quasicircular configurations with a nonspinning smaller mass black hole (labeled 1) and a larger mass spinning black hole (labeled 2). The punctures are located at $\vec{r}_1 = (x_1, 0, 0)$ and $\vec{r}_2 = (x_2, 0, 0)$, with momenta $P = \pm(0, P, 0)$, spins $\vec{S}_i = (0, 0, S_i)$, mass parameters m^p/m, horizon (Christodoulou) masses m^H/m, total Arnowitt-Deser-Misner (ADM) mass M_{ADM}, and dimensionless spins $a/m_H = S/m_H^2$. The configurations are denoted by QX_Y_Z, where X gives the mass ratio m_1^H/m_2^H, Y gives the spin of the smaller BH (a_1/m_H^2), and Z gives the spin of the larger BH (a_2/m_H^2).

Configuration	x_1/m	x_2/m	P/m	m_1^p/m	m_2^p/m	S_1/m^2	S_2/m^2	m_1^H/m	m_2^H/m	M_{ADM}/m	a_1/m_1^H	a_2/m_2^H
Q1.000_0.00_0.00	−4.7666	4.7666	0.099322	0.48523	0.48523	0	0	0.5	0.5	0.98931	0	0
Q1.000_0.00_0.40	−4.6378	4.523	0.1004	0.48472	0.45144	0	0.1	0.5	0.5	0.9888	0	0.4
Q1.000_0.00_0.60	−4.5759	4.4035	0.10101	0.48445	0.40145	0	0.15	0.5	0.5	0.9886	0	0.6
Q1.000_0.00_0.80	−4.5152	4.2852	0.10159	0.48418	0.30103	0	0.2	0.5	0.5	0.98842	0	0.8
Q1.000_0.20_0.80	−4.4307	4.3878	0.10071	0.47635	0.30108	0.05	0.2	0.5	0.5	0.98838	0.2	0.8
Q1.000_0.40_−0.40	−5.0346	4.9785	0.095751	0.45266	0.45259	−0.1	0.1	0.5	0.5	0.98971	−0.4	0.4
Q1.000_0.40_0.80	−4.405	4.3766	0.10025	0.45098	0.30107	0.1	0.2	0.5	0.5	0.98829	0.4	0.8
Q1.000_−0.60_0.60	−4.8029	4.7172	0.09907	0.40219	0.4021	−0.15	0.15	0.5	0.5	0.98937	−0.6	0.6
Q1.000_−0.80_0.80	−4.9832	4.5267	0.09905	0.30178	0.30168	−0.2	0.2	0.5	0.5	0.98951	−0.8	0.8
Q0.750_0.00_−0.25	−6.0062	4.5158	0.091564	0.41524	0.54417	0	−0.081633	0.42857	0.57143	0.99034	0	−0.25
Q0.750_−0.80_0.45	−5.7814	4.2576	0.094019	0.25784	0.50845	−0.14694	0.14694	0.42857	0.57143	0.99011	−0.8	0.45
Q0.750_0.80_−0.45	−5.6572	4.308	0.093655	0.25774	0.50848	0.14694	−0.14694	0.42857	0.57143	0.98998	0.8	−0.45
Q0.750_−0.80_−0.60	−6.2721	4.6997	0.091817	0.25847	0.46326	−0.14694	−0.19592	0.42857	0.57143	0.99111	−0.8	−0.6
Q0.750_0.80_0.60	−5.05	3.7787	0.097289	0.25676	0.46102	0.14694	0.19592	0.42857	0.57143	0.98858	0.8	0.6
Q0.750_0.80_−0.80	−6.1633	4.7098	0.089327	0.25845	0.34767	0.14694	−0.26122	0.42857	0.57143	0.99083	0.8	−0.8
Q0.500_0.00_−0.50	−6.9641	3.5416	0.084316	0.32093	0.58184	0	−0.22222	0.33333	0.66667	0.99136	0	−0.5
Q0.500_0.00_0.50	−6.2598	3.1299	0.087209	0.31969	0.58068	0	0.22222	0.33333	0.66667	0.99027	0	0.5
Q0.500_−0.80_0.20	−6.6141	3.2581	0.086691	0.19907	0.64372	−0.088889	0.088889	0.33333	0.66667	0.99096	−0.8	0.2
Q0.500_0.80_−0.20	−6.487	3.2681	0.086176	0.19898	0.64368	0.088889	−0.088889	0.33333	0.66667	0.99076	0.8	−0.2
Q0.500_−0.80_−0.40	−6.682	3.3317	0.088305	0.19909	0.60963	−0.088889	−0.17778	0.33333	0.66667	0.9913	−0.8	−0.4
Q0.500_0.80_0.40	−5.9213	2.9452	0.089199	0.19825	0.60838	0.088889	0.17778	0.33333	0.66667	0.9898	0.8	0.4
Q0.500_−0.80_−0.80	−7.3137	3.674	0.083939	0.19978	0.4078	−0.088889	−0.35556	0.33333	0.66667	0.99207	−0.8	−0.8
Q0.500_−0.80_0.80	−6.0831	2.6801	0.091117	0.19815	0.4061	−0.088889	0.35556	0.33333	0.66667	0.98988	−0.8	0.8
Q0.500_0.80_−0.80	−7.0541	3.8437	0.081882	0.19978	0.40782	0.088889	−0.35556	0.33333	0.66667	0.99179	0.8	−0.8
Q0.500_0.80_0.80	−5.7338	2.8246	0.089267	0.19801	0.40601	0.088889	0.35556	0.33333	0.66667	0.98938	0.8	0.8
Q0.333_0.00_−0.67	−7.8557	2.6696	0.07199	0.23933	0.57549	0	−0.375	0.25	0.75	0.99283	0	−0.66667
Q0.333_0.00_0.67	−6.8651	2.2087	0.074136	0.23799	0.57436	0	0.375	0.25	0.75	0.99145	0	0.66667
Q0.333_−0.80_0.80	−6.545	1.8547	0.078325	0.14731	0.45916	−0.05	0.45	0.25	0.75	0.99112	−0.8	0.8
Q0.333_0.80_−0.80	−7.7455	2.8644	0.071192	0.1488	0.46071	0.05	−0.45	0.25	0.75	0.99301	0.8	−0.8
Q0.250_0.00_−0.75	−8.7925	2.2393	0.059859	0.19121	0.54795	0	−0.48	0.2	0.8	0.99415	0	−0.75
Q0.250_0.00_0.75	−7.0934	1.7028	0.064078	0.18938	0.54664	0	0.48	0.2	0.8	0.9925	0	0.75
Q0.250_0.80_−0.80	−8.4636	2.1489	0.061171	0.11861	0.49276	0.032	−0.512	0.2	0.8	0.99409	0.8	−0.8
Q0.200_0.00_−0.80	−9.4341	1.9209	0.051156	0.15919	0.51448	0	−0.55556	0.16667	0.83333	0.99506	0	−0.8
Q0.200_0.00_0.80	−7.2578	1.3894	0.055956	0.15726	0.51325	0	0.55556	0.16667	0.83333	0.99338	0	0.8
Q0.167_0.00_−0.83	−9.0003	1.5299	0.04788	0.1357	0.47918	0	−0.61224	0.14286	0.85714	0.99542	0	−0.83333
Q0.167_0.00_0.83	−7.2953	1.2159	0.049656	0.13442	0.4784	0	0.61224	0.14286	0.85714	0.99408	0	0.83333
Q0.100_0.00_0.00[a]	7.6331	−0.7532	0.036699	0.08524	0.90740	0	0	0.09129	0.91255	1.0000	0	0

[a]Note that the $q = 1/10$ binary also had an initial radial momentum of $P_r/m = -0.0001685$.

To generate the initial data parameters, we use 3PN quasicircular orbital parameters with a given initial orbital frequency ω_i. In practice, this leads to an initial eccentricity of the order of $e_i \sim 10^{-2}$ that radiates after a few orbits to about $e_f \sim 5 \times 10^{-3}$, which is small enough for modeling the remnant in astrophysical applications [58]. Tables I–III provides explicit values for all the initial data parameters used in each of the runs presented in this paper. We also provide the initial and final eccentricity and total number of orbits in the table.

We evolve these data sets using the grid refinement structure and global resolution discussed in Appendix A. In this appendix, we also describe in detail the errors in our results due to finite extraction radii and finite truncation errors, as well as how we extrapolate from finite radii to null infinity.

In order to cover the three-dimensional parameter space of the aligned-spin BHBs, we consider several families of physically motivated configurations. We denote our configurations by XY, where X = U, D, or 0 denotes the spin of the smaller BH (i.e., aligned, counteraligned, or zero) and Y denotes the spin of the larger BH. If accretion tends to align the spins, then the UD, DU, UU, and DD configurations should be among the most probable. The 0U and 0D configurations, depicted in Fig. 2, are interesting in that if the recoil as given in Eq. (2b) is dominated by the leading $\Delta_\parallel$ dependence, then a 0U or 0D configuration is an effective counterpart to a UU or DD configuration where both BHs are spinning with the same dimensionless spin α and $\alpha_{\rm Effective} = \pm(1-q)\alpha'$ (i.e., a 0U with spin $\alpha_{\rm Effective}$ should give the same recoil as a UU/DD configuration with $\alpha_2 = \alpha_1 = \alpha'$). Since $\alpha_{\rm Effective}$ is smaller than α', we can apparently simulate maximal UU and DD configurations with nonmaximal 0U and 0D configurations. We thus study BHBs with the smaller BH nonspinning and the larger BH spinning with spin

TABLE II. The mass and spin of the BHBs in Table I after the BHs had time to equilibrate ($t/M = 150$).

Configuration	m_1^r/m	m_2^r/m	α_1^r	α_2^r	δm_r	S_r/m_r^2	Δ_r/m_r^2
Q1.000_0.00_0.00	0.500001	0.500001	−0.000002	−0.000002	0.000000	−0.000001	0.000000
Q1.000_0.00_0.40	0.499998	0.500005	−0.000002	0.399919	−0.000007	0.099981	0.199962
Q1.000_0.00_0.60	0.499998	0.499975	−0.000002	0.600030	0.000023	0.150000	0.300009
Q1.000_0.00_0.80	0.499999	0.499804	−0.000001	0.800605	0.000195	0.200073	0.400225
Q1.000_0.20_0.80	0.500006	0.499804	0.199991	0.800585	0.000202	0.250083	0.300196
Q1.0000.40_ − 0.40	0.500006	0.500007	−0.400013	0.399986	−0.000001	−0.000006	0.399999
Q1.000_0.40_0.80	0.500009	0.499803	0.399974	0.800587	0.000206	0.300099	0.200183
Q1.000_ − 0.60_0.60	0.499976	0.499980	−0.600096	0.600029	−0.000004	−0.000014	0.600063
Q1.000_ − 0.80_0.80	0.499801	0.499808	−0.800702	0.800576	−0.000007	−0.000026	0.800639
Q0.750_0.00_ − 0.25	0.428573	0.571432	−0.000002	−0.250015	−0.142858	−0.081638	−0.142865
Q0.750_ − 0.80_0.45	0.428415	0.571439	−0.800654	0.449990	−0.143045	−0.000011	0.600241
Q0.750_0.80_ − 0.45	0.428417	0.571428	0.800563	−0.450042	−0.143033	−0.000016	−0.600235
Q0.750_ − 0.80_ − 0.60	0.428413	0.571397	−0.800656	−0.600070	−0.143011	−0.343001	0.000133
Q0.750_0.80_0.60	0.428422	0.571391	0.800523	0.600059	−0.142995	0.342972	−0.000093
Q0.750_0.80_ − 0.80	0.428412	0.571165	0.800579	−0.800777	−0.142813	−0.114398	−0.800692
Q0.500_0.00_ − 0.50	0.333333	0.666646	−0.000003	−0.500057	−0.333320	−0.222243	−0.333367
Q0.500_0.00_0.50	0.333333	0.666647	−0.000003	0.500073	−0.333321	0.222250	0.333380
Q0.500_ − 0.80_0.20	0.333239	0.666684	−0.800560	0.199993	−0.333471	−0.000010	0.400141
Q0.500_0.80_ − 0.20	0.333239	0.666670	0.800469	−0.200003	−0.333462	−0.000001	−0.400120
Q0.500_ − 0.80_ − 0.40	0.333243	0.666681	−0.800542	−0.399969	−0.333463	−0.266713	0.000124
Q0.500_0.80_0.40	0.333244	0.666666	0.800412	0.400002	−0.333452	0.266713	−0.000065
Q0.500_ − 0.80_ − 0.80	0.333233	0.666348	−0.800574	−0.800723	−0.333254	−0.444809	−0.266894
Q0.500_ − 0.80_0.80	0.333246	0.666358	−0.800499	0.800638	−0.333244	0.266823	0.800592
Q0.500_0.80_ − 0.80	0.333232	0.666330	0.800530	−0.800798	−0.333244	−0.266891	−0.800708
Q0.500_0.80_0.80	0.333245	0.666344	0.800398	0.800701	−0.333237	0.444774	0.266924
Q0.333_0.00_ − 0.67	0.249994	0.749857	−0.000002	−0.666947	−0.499938	−0.375127	−0.500189
Q0.333_0.00_0.67	0.249997	0.749855	−0.000004	0.666920	−0.499931	0.375108	0.500168
Q0.333_ − 0.80_0.80	0.249953	0.749624	−0.800179	0.800758	−0.499883	0.400322	0.800613
Q0.333_0.80_ − 0.80	0.249944	0.749607	0.800395	−0.800865	−0.499888	−0.400372	−0.800748
Q0.250_0.00_ − 0.75	0.200004	0.799697	−0.000002	−0.750583	−0.599873	−0.480297	−0.600419
Q0.250_0.00_0.75	0.199998	0.799695	−0.000003	0.750566	−0.599881	0.480291	0.600408
Q0.250_0.80_ − 0.80	0.199967	0.799568	0.800375	−0.800890	−0.599880	−0.480459	−0.800787
Q0.200_0.00_ − 0.80	0.166673	0.832872	0.000001	−0.800897	−0.666502	−0.556069	−0.667348
Q0.200_0.00_0.80	0.166665	0.832869	0.000004	0.800884	−0.666515	0.556068	0.667342
Q0.167_0.00_ − 0.83	0.142855	0.856538	−0.000002	−0.834514	−0.714117	−0.612992	−0.715227
Q0.167_0.00_0.83	0.142855	0.856533	−0.000001	0.834513	−0.714115	0.612989	0.715226

$\alpha_{\rm Effective} = \pm(1-q)$ for $q = 1/2, 1/3, 1/4, 1/5, 1/6$. A first analysis of those simulations suggested that although leading, the $\Delta_\parallel$ dependence in Eq. (2b) is not sufficient to model the recoils with high accuracy. We thus consider additional families (see Fig. 3) of BHBs, with specific spins $\alpha \leq 0.8$ in a UD or DU configuration. In addition to showing the importance of the total spin $S_\parallel$ to the recoil, we also found from these configurations that the maximum recoil occurs for $q_{\rm max} \sim 0.62$, as shown in Fig. 4.

We chose other configurations to selectively activate or deactivate blocks of terms in the expansion formulas for the recoil and radiated energy momentum. Thus, some simulations have only one of the variables δm, $S_\parallel$, and $\Delta_\parallel$ nonvanishing and others have all of them nonvanishing. This provides a means of fitting all terms and then verifying the fit for more general cases. The complete set of initial data parameters are given in Table I. In the table, the runs are labeled by the mass ratio, spin magnitude of black hole 1 (the smaller BH), and spin magnitude of black hole 2 (the larger BH).

Since the initial data assume conformal flatness and pure longitudinal extrinsic curvature, they contain initial distortions that are either radiated away or absorbed by the BHs during the first orbital period. After this initial transient period, the BH masses and spins settle to their equilibrium values. In Table II we give the values for the horizon mass and spin after this transient period has ended.

After the BHs in the progenitor BHB merge, we measure the remnants mass, spin, and recoil velocity. We measure the recoil velocity from the radiation of linear momentum at infinity, as this is the most reliable and gauge invariant way of computing recoils. The resulting recoil velocities are given in Table IV. In order to produce accurate results, we extracted the waveform at different finite radii and extrapolated to infinity. Here we chose observer locations equidistant in $1/r$, where the largest extraction radius was $102.6m$. We fit the finite-radius results for the recoil, energy radiated, and angular momentum radiated to linear and quadratic functions in $1/r$, and we use the difference between these two fits as an estimate for the error due to finite radius, which we report in the table. As we discuss in Appendix A, other sources of error come from the finite numerical resolution and the maximum ℓ mode used in the extraction. Based on our assessment of those errors (see Appendix A), we compute the recoil using the $\ell = 2$ through $\ell = 6$ modes. Also based on the results in Appendix A, we estimate the truncation error in the recoil to be $\sim 10\ {\rm km\,s^{-1}}$.

In Table V we give the horizon mass and spin magnitude of the remnant BH for each configuration studied here. We measure these using the isolated horizon formalism and based on the measured radiated mass and angular momentum. However, the isolated horizon measurements are expected to be more accurate, and the differences between the isolated horizon and radiation quantities are largely due to truncation errors in the radiation zone that do not affect the accuracy near the horizons themselves (see Ref. [59]). As shown in Appendix A, the truncation errors in the isolated horizon measurements are quite small. Note that the errors reported in the table do not include truncation errors. From the results in Appendix A, we estimate that the truncation error in the isolated horizon measure of $\delta\mathcal{M}$ is $\sim 10^{-5}$, while the error in $\alpha_{\rm rem}$ is $\sim 10^{-4}$.

TABLE III. Table of the initial orbital frequency $m\omega_i$, number of orbits to merger, N, and the initial and final eccentricities, e_i and e_f.

Configuration	$m\omega_i$	N	e_i	e_f
Q1.000_0.00_0.00	0.0300	5.3	0.028	0.005
Q1.000_0.00_0.40	0.0313	5.4	0.021	0.006
Q1.000_0.00_0.60	0.0320	5.6	0.021	0.005
Q1.000_0.00_0.80	0.0327	5.7	0.020	0.004
Q1.000_0.20_0.80	0.0324	6.2	0.020	0.002
Q1.000_0.40_−0.40	0.0280	5.9	0.023	0.002
Q1.000_0.40_0.80	0.0324	6.6	0.020	0.002
Q1.000_−0.60_0.60	0.0300	5.1	0.022	0.005
Q1.000_−0.80_0.80	0.0300	5.1	0.022	0.005
Q0.750_0.00_−0.25	0.0263	6.2	0.024	0.005
Q0.750_−0.80_0.45	0.0280	5.7	0.022	0.003
Q0.750_0.80_−0.45	0.0280	6.1	0.023	0.006
Q0.750_−0.80_−0.60	0.0254	4.6	0.024	0.005
Q0.750_0.80_0.60	0.0320	7.1	0.020	0.004
Q0.750_0.80_−0.80	0.0250	6.6	0.025	0.005
Q0.500_0.00_−0.50	0.0265	5.4	0.020	0.005
Q0.500_0.00_0.50	0.0300	7.2	0.024	0.003
Q0.500_−0.80_0.20	0.0287	5.6	0.019	0.003
Q0.500_0.80_−0.20	0.0287	6.2	0.019	0.005
Q0.500_−0.80_−0.40	0.0287	4.0	0.018	0.004
Q0.500_0.80_0.40	0.0320	6.8	0.018	0.004
Q0.500_−0.80_−0.80	0.0254	4.1	0.019	0.008
Q0.500_−0.80_0.80	0.0330	6.1	0.017	0.002
Q0.500_0.80_−0.80	0.0250	6.1	0.021	0.005
Q0.500_0.80_0.80	0.0330	7.8	0.017	0.002
Q0.333_0.00_−0.67	0.0265	5.0	0.013	0.008
Q0.333_0.00_0.67	0.0310	8.6	0.014	0.003
Q0.333_−0.80_0.80	0.0345	7.1	0.012	0.003
Q0.333_0.80_−0.80	0.0260	5.3	0.014	0.006
Q0.250_0.00_−0.75	0.0248	5.7	0.014	0.005
Q0.250_0.00_0.75	0.0320	10.1	0.011	0.003
Q0.250_0.80_−0.80	0.0260	5.2	0.009	0.008
Q0.200_0.00_−0.80	0.0238	6.4	0.015	0.006
Q0.200_0.00_0.80	0.0325	11.3	0.011	0.002
Q0.167_0.00_−0.83	0.0265	4.4	0.014	0.008
Q0.167_0.00_0.83	0.0330	12.8	0.010	0.002

IV. NEW MODELS OF REMNANT MASS, SPIN, AND RECOIL

In Refs. [8] and [59] we developed a series expansion for the mass, spin, and recoil velocity of the remnant BH

TABLE IV. The recoil velocity as calculated using $\ell_{\rm max} = 6$ and $r_{\rm max} = 102.6m$. The error estimates are due to radial extrapolation errors. We estimate that the finite difference errors are of order 10 km s^{-1} (see Appendix A for more details)

Run	Configuration	V_x	V_y	V
1	Q1.000_0.00_0.00	0.0 ± 0.0	0.0 ± 0.0	0.0 ± 0.0
2	Q1.000_0.00_0.40	-24.36 ± 1.16	-80.37 ± 0.23	83.97 ± 0.40
3	Q1.000_0.00_0.60	54.72 ± 1.65	-104.99 ± 1.92	118.40 ± 1.87
4	Q1.000_0.00_0.80	141.16 ± 0.52	-39.33 ± 4.57	146.53 ± 1.32
5	Q1.000_0.20_0.80	-76.92 ± 2.28	60.74 ± 0.52	98.01 ± 1.82
6	Q1.000_0.40_−0.40	82.56 ± 2.39	164.52 ± 1.12	184.07 ± 1.47
7	Q1.000_0.40_0.80	4.99 ± 0.84	-53.98 ± 0.69	54.22 ± 0.69
8	Q1.000_−0.60_0.60	-209.74 ± 2.12	177.56 ± 2.07	274.80 ± 2.10
9	Q1.000_−0.80_0.80	-167.03 ± 3.96	327.50 ± 1.27	367.63 ± 2.13
10	Q0.750_0.00_−0.25	105.53 ± 0.49	-86.34 ± 0.67	136.35 ± 0.57
11	Q0.750_−0.80_0.45	208.49 ± 0.25	60.82 ± 6.60	217.18 ± 1.86
12	Q0.750_0.80_−0.45	166.34 ± 1.33	-271.75 ± 0.25	318.61 ± 0.73
13	Q0.750_−0.80_−0.60	15.40 ± 1.42	94.31 ± 0.79	95.57 ± 0.81
14	Q0.750_0.80_0.60	3.89 ± 1.57	-27.08 ± 0.27	27.36 ± 0.35
15	Q0.750_0.80_−0.80	-333.94 ± 1.70	258.31 ± 4.36	422.19 ± 2.99
16	Q0.500_0.00_−0.50	155.44 ± 1.36	222.33 ± 1.06	271.28 ± 1.17
17	Q0.500_0.00_0.50	-18.50 ± 1.66	-34.08 ± 5.12	38.77 ± 4.56
18	Q0.500_−0.80_0.20	62.47 ± 2.45	66.40 ± 6.26	91.16 ± 4.86
19	Q0.500_0.80_−0.20	254.30 ± 0.10	-68.79 ± 2.32	263.43 ± 0.61
20	Q0.500_−0.80_−0.40	-120.44 ± 2.83	-128.91 ± 0.01	176.42 ± 1.93
21	Q0.500_0.80_0.40	-80.19 ± 0.19	-8.70 ± 1.76	80.67 ± 0.26
22	Q0.500_−0.80_−0.80	126.69 ± 1.08	-235.55 ± 1.65	267.46 ± 1.54
23	Q0.500_−0.80_0.80	59.84 ± 6.28	142.31 ± 11.19	154.38 ± 10.60
24	Q0.500_0.80_−0.80	231.96 ± 0.78	-350.71 ± 2.17	420.48 ± 1.86
25	Q0.500_0.80_0.80	2.12 ± 4.77	-0.39 ± 2.11	2.15 ± 4.71
26	Q0.333_0.00_−0.67	-127.75 ± 2.03	-257.15 ± 0.57	287.15 ± 1.04
27	Q0.333_0.00_0.67	23.02 ± 2.89	-9.61 ± 1.69	24.94 ± 2.74
28	Q0.333_−0.80_0.80	20.09 ± 4.71	69.37 ± 8.74	72.22 ± 8.50
29	Q0.333_0.80_−0.80	346.95 ± 1.00	21.11 ± 1.57	347.60 ± 1.01
30	Q0.250_0.00_−0.75	-200.80 ± 0.04	143.20 ± 1.07	246.63 ± 0.62
31	Q0.250_0.00_0.75	3.53 ± 2.91	11.09 ± 5.46	11.64 ± 5.27
32	Q0.250_0.80_−0.80	254.96 ± 0.06	-95.67 ± 1.83	272.32 ± 0.65
33	Q0.200_0.00_−0.80	199.51 ± 0.62	46.95 ± 1.27	204.97 ± 0.67
34	Q0.200_0.00_0.80	-1.18 ± 5.14	-3.20 ± 1.49	3.41 ± 2.27
35	Q0.167_0.00_−0.83	171.27 ± 0.72	9.26 ± 1.27	171.52 ± 0.73
36	Q0.167_0.00_0.83	3.33 ± 3.27	0.51 ± 0.29	3.37 ± 3.23

produced by the merger of a progenitor BHB with arbitrary BH spin magnitudes and orientations and arbitrary mass ratio in terms of the variables $\vec{\Delta}$, $\vec{S}$, and δm. For the runs presented here, only terms proportional to $S_\parallel$, $\Delta_\parallel$, and δm contribute. In addition, only certain combinations are allowed by symmetry considerations. For more details see Table IV of Ref. [8] and Table VI of Ref. [59]. Here we include all allowed terms up through fourth order. We include powers of δm when counting orders. This differs from our previous conventions [8,59], where we only counted powers in the spin variables and allowed the coefficients of those terms to be arbitrary functions of δm (consistent with the symmetries).

The formula for the mass of the remnant $M_{\rm rem}$ is then given by

$$\begin{aligned}\frac{M_{\rm rem}}{m} = \{&M_0 + K_1\tilde{S}_\parallel + K_{2a}\tilde{\Delta}_\parallel\delta m + K_{2b}\tilde{S}_\parallel^2 + K_{2c}\tilde{\Delta}_\parallel^2 + K_{2d}\delta m^2 + K_{3a}\tilde{\Delta}_\parallel\tilde{S}_\parallel\delta m + K_{3b}\tilde{S}_\parallel\tilde{\Delta}_\parallel^2 \\ &+ K_{3c}\tilde{S}_\parallel^3 + K_{3d}\tilde{S}_\parallel\delta m^2 + K_{4a}\tilde{\Delta}_\parallel\tilde{S}_\parallel^2\delta m + K_{4b}\tilde{\Delta}_\parallel^3\delta m + K_{4c}\tilde{\Delta}_\parallel^4 + K_{4d}\tilde{S}_\parallel^4 + K_{4e}\tilde{\Delta}_\parallel^2\tilde{S}_\parallel^2 \\ &+ K_{4f}\delta m^4 + K_{4g}\tilde{\Delta}_\parallel\delta m^3 + K_{4h}\tilde{\Delta}_\parallel^2\delta m^2 + K_{4i}\tilde{S}_\parallel^2\delta m^2\} + \mathcal{O}(\epsilon^5),\end{aligned} \tag{13}$$

where $\mathcal{O}(\epsilon^5)$ denotes terms of fifth and higher order in the expansion variables and where variables with tildes are dimensionless, that is, $\tilde{S}_\parallel = S_\parallel/m^2$ and $\tilde{\Delta}_\parallel = \Delta_\parallel/m^2$. As written, Eq. (13) does not reproduce exactly the particle limit since $\delta m \to \pm 1$ as $\eta \to 0$. However, we can add terms of order $\mathcal{O}(\epsilon^6)$ and higher to obtain the correct particle limit behavior while simultaneously producing an expansion equivalent to Eq. (13). First, we note that in the particle limit, $M_{\rm rem}$ is given by $M_{\rm rem}/m = 1 + \eta(\tilde{E}_{\rm isco} - 1) + \mathcal{O}(\eta)^2$ (where $m\eta\tilde{E}_{\rm isco}$ is the energy of a particle at the inner-most stable circular orbit (ISCO). To enforce the particle limit for zero spin, we add two terms, $K_6\delta m^6 + K_8\delta m^8$, and then fix the value of these constants by demanding that a reexpansion in terms of η gives $1 + \eta(\tilde{E}^{\rm sch}_{\rm isco} - 1) + \mathcal{O}(\eta)^2$ ($\tilde{E}^{\rm sch}_{\rm isco}$ is the Schwarzschild ISCO energy). We follow a similar procedure for the spin-dependent terms. For most terms in Eq. (13), the net effect is to simply multiply the given term by $(4\eta)^2$. The resulting formula for $M_{\rm rem}$ is given by

$$\begin{aligned}\frac{M_{\rm rem}}{m} = (4\eta)^2\{&M_0 + K_1\tilde{S}_\parallel + K_{2a}\tilde{\Delta}_\parallel\delta m + K_{2b}\tilde{S}_\parallel^2 + K_{2c}\tilde{\Delta}_\parallel^2 + K_{2d}\delta m^2 + K_{3a}\tilde{\Delta}_\parallel\tilde{S}_\parallel\delta m + K_{3b}\tilde{S}_\parallel\tilde{\Delta}_\parallel^2 + K_{3c}\tilde{S}_\parallel^3 \\ &+ K_{3d}\tilde{S}_\parallel\delta m^2 + K_{4a}\tilde{\Delta}_\parallel\tilde{S}_\parallel^2\delta m + K_{4b}\tilde{\Delta}_\parallel^3\delta m + K_{4c}\tilde{\Delta}_\parallel^4 + K_{4d}\tilde{S}_\parallel^4 + K_{4e}\tilde{\Delta}_\parallel^2\tilde{S}_\parallel^2 + K_{4f}\delta m^4 + K_{4g}\tilde{\Delta}_\parallel\delta m^3 \\ &+ K_{4h}\tilde{\Delta}_\parallel^2\delta m^2 + K_{4i}\tilde{S}_\parallel^2\delta m^2\} + [1 + \eta(\tilde{E}_{\rm ISCO} + 11)]\delta m^6. \end{aligned} \tag{14}$$

Here we take $\tilde{E}_{\rm ISCO}$ from Eq. (2.7) of Ref. [60] (we replace the variable a in Ref. [60] with $\alpha_{\rm rem}$, but similar results are obtained when using $S_\parallel/m^2$ instead).

We then verified that the correct leading power of 4η in Eq. (14) is indeed 2 by replacing $(4\eta)^2$ with $(4\eta)^p$ and fitting all coefficients, and we found that $p = 2.0006$ gives the best fit. In Table VI the power p is set to 2 exactly when performing the fits.

To obtain a phenomenological formula for the remnant spin, we follow a similar procedure. Prior to enforcing the particle limit we have

$$\begin{aligned}\alpha_{\rm rem} = \frac{S_{\rm rem}}{M_{\rm rem}^2} = \{&L_0 + L_1\tilde{S}_\parallel + L_{2a}\tilde{\Delta}_\parallel\delta m + L_{2b}\tilde{S}_\parallel^2 + L_{2c}\tilde{\Delta}_\parallel^2 + L_{2d}\delta m^2 + L_{3a}\tilde{\Delta}_\parallel\tilde{S}_\parallel\delta m + L_{3b}\tilde{S}_\parallel\tilde{\Delta}_\parallel^2 + L_{3c}\tilde{S}_\parallel^3 \\ &+ L_{3d}\tilde{S}_\parallel\delta m^2 + L_{4a}\tilde{\Delta}_\parallel\tilde{S}_\parallel^2\delta m + L_{4b}\tilde{\Delta}_\parallel^3\delta m + L_{4c}\tilde{\Delta}_\parallel^4 + L_{4d}\tilde{S}_\parallel^4 + L_{4e}\tilde{\Delta}_\parallel^2\tilde{S}_\parallel^2 + L_{4f}\delta m^4 + L_{4g}\tilde{\Delta}_\parallel\delta m^3 \\ &+ L_{4h}\tilde{\Delta}_\parallel^2\delta m^2 + L_{4i}\tilde{S}_\parallel^2\delta m^2\} + \mathcal{O}(\epsilon^5). \end{aligned} \tag{15}$$

Once again, we add higher-order terms in order to enforce the correct particle limit behavior. Here the new terms are generated by multiplying the existing terms in Eq. (15) by the next even powers of δm that correspond to $\mathcal{O}(\epsilon^5)$ or higher. For instance, for the spin-independent terms we add $L_6\delta m^6 + L_8\delta m^8$, and for the linear in the spin terms, $L_5 S_\parallel\delta m^4 + L_7 S_\parallel\delta m^6$. We then impose the particle limit, which is given by $\alpha_{\rm rem} = \tilde{S}_\parallel + \eta\tilde{J}_{\rm ISCO} + \mathcal{O}(\eta^2)$. Again, we use Eq. (2.8) of Ref. [60] to calculate the ISCO angular momentum, replacing the variable a there with $\alpha_{\rm rem}$.

After enforcing the particle limit, we get

$$\begin{aligned}\alpha_{\rm rem} = \frac{S_{\rm rem}}{M_{\rm rem}^2} = (4\eta)^2\{&L_0 + L_1\tilde{S}_\parallel + L_{2a}\tilde{\Delta}_\parallel\delta m + L_{2b}\tilde{S}_\parallel^2 + L_{2c}\tilde{\Delta}_\parallel^2 + L_{2d}\delta m^2 + L_{3a}\tilde{\Delta}_\parallel\tilde{S}_\parallel\delta m + L_{3b}\tilde{S}_\parallel\tilde{\Delta}_\parallel^2 + L_{3c}\tilde{S}_\parallel^3 \\ &+ L_{3d}\tilde{S}_\parallel\delta m^2 + L_{4a}\tilde{\Delta}_\parallel\tilde{S}_\parallel^2\delta m + L_{4b}\tilde{\Delta}_\parallel^3\delta m + L_{4c}\tilde{\Delta}_\parallel^4 + L_{4d}\tilde{S}_\parallel^4 + L_{4e}\tilde{\Delta}_\parallel^2\tilde{S}_\parallel^2 + L_{4f}\delta m^4 + L_{4g}\tilde{\Delta}_\parallel\delta m^3 \\ &+ L_{4h}\tilde{\Delta}_\parallel^2\delta m^2 + L_{4i}\tilde{S}_\parallel^2\delta m^2\} + \tilde{S}_\parallel(1 + 8\eta)\delta m^4 + \eta\tilde{J}_{\rm ISCO}\delta m^6. \end{aligned} \tag{16}$$

In order to verify our hypothesis, we first replace $(4\eta)^2$ with $(4\eta)^p$ and fit for all coefficients in Eq. (16). We find $p = 2.015$, which is reasonably close to the expected power of 2. We then fit again using $p = 2$ exactly and report these fitting parameters in Table VI.

By using $a = \alpha_{\rm rem}$ to evaluate the ISCO quantities, the fitting formula for the spin becomes implicit, and the formula for the mass depends directly on the formula for the spin. Therefore, to evaluate the fitting formulas for any given initial binary, we use a rapidly converging iterative process where the initial a is set to $S_\parallel/m^2$.

Finally, we fit the recoil to the formula

$$\begin{aligned}v_\perp = H\eta^2(&\tilde{\Delta}_\parallel + H_{2a}\tilde{S}_\parallel\delta m + H_{2b}\tilde{\Delta}_\parallel\tilde{S}_\parallel + H_{3a}\tilde{\Delta}_\parallel^2\delta m \\ &+ H_{3b}\tilde{S}_\parallel^2\delta m + H_{3c}\tilde{\Delta}_\parallel\tilde{S}_\parallel^2 + H_{3d}\tilde{\Delta}_\parallel^3 + H_{3e}\tilde{\Delta}_\parallel\delta m^2 \\ &+ H_{4a}\tilde{S}_\parallel\tilde{\Delta}_\parallel^2\delta m + H_{4b}\tilde{S}_\parallel^3\delta m + H_{4c}\tilde{S}_\parallel\delta m^3 \\ &+ H_{4d}\tilde{\Delta}_\parallel\tilde{S}_\parallel\delta m^2 + H_{4e}\tilde{\Delta}_\parallel\tilde{S}_\parallel^3 + H_{4f}\tilde{S}_\parallel\tilde{\Delta}_\parallel^3), \end{aligned} \tag{17}$$

TABLE V. The final remnant mass and spin as measured using the IH formalism and as measured from the radiation of energy and angular momentum. The error bars in the radiative quantities are due to radial extrapolation errors, while the error bars in the IH quantities are due to variations in the measured mass and spin with time. See Appendix A for estimates of the truncation error. The expected truncation error in $\delta\mathcal{M}_{\rm IH}$ is 10^{-5}, and the error in $\alpha_{\rm IH}$ is 10^{-4}.

Run	Configuration	$\delta\mathcal{M}^{IH}$	$\delta\mathcal{M}^{\rm rad}$	$\alpha^{IH}_{\rm rem}$	$\alpha^{\rm rad}_{\rm rem}$
1	Q1.000_0.00_0.00	0.048379 ± 0.000001	0.047937 ± 0.000177	0.686419 ± 0.000007	0.685034 ± 0.004747
2	Q1.000_0.00_0.40	0.054557 ± 0.000002	0.053888 ± 0.000190	0.745985 ± 0.000058	0.745180 ± 0.004325
3	Q1.000_0.00_0.60	0.058316 ± 0.000004	0.057438 ± 0.000250	0.774671 ± 0.000195	0.774270 ± 0.004519
4	Q1.000_0.00_0.80	0.062821 ± 0.000007	0.061610 ± 0.000362	0.802619 ± 0.000086	0.802453 ± 0.004977
5	Q1.000_0.20_0.80	0.067692 ± 0.000001	0.066171 ± 0.000443	0.830671 ± 0.000015	0.830647 ± 0.005519
6	Q1.000_0.40_−0.40	0.048437 ± 0.000000	0.047998 ± 0.000163	0.685844 ± 0.000001	0.683873 ± 0.005278
7	Q1.000_0.40_0.80	0.073515 ± 0.000003	0.071532 ± 0.000572	0.857465 ± 0.000046	0.857999 ± 0.006244
8	Q1.000_−0.60_0.60	0.048780 ± 0.000000	0.048268 ± 0.000202	0.685258 ± 0.000000	0.683850 ± 0.004611
9	Q1.000_−0.80_0.80	0.049353 ± 0.000000	0.048593 ± 0.000304	0.684235 ± 0.000020	0.682995 ± 0.005103
10	Q0.750_0.00_−0.25	0.042681 ± 0.000009	0.042368 ± 0.000179	0.621171 ± 0.000025	0.618973 ± 0.006118
11	Q0.750_−0.80_0.45	0.046525 ± 0.000001	0.045794 ± 0.000280	0.685173 ± 0.000021	0.684202 ± 0.005942
12	Q0.750_0.80_−0.45	0.047283 ± 0.000001	0.046683 ± 0.000270	0.662124 ± 0.000027	0.660424 ± 0.006072
13	Q0.750_−0.80_−0.60	0.033808 ± 0.000000	0.033435 ± 0.000204	0.451036 ± 0.000001	0.449575 ± 0.005390
14	Q0.750_0.80_0.60	0.075774 ± 0.000000	0.073304 ± 0.000761	0.871698 ± 0.000003	0.872990 ± 0.007658
15	Q0.750_0.80_−0.80	0.042577 ± 0.000000	0.042037 ± 0.000329	0.586122 ± 0.000000	0.584030 ± 0.007777
16	Q0.500_0.00_−0.50	0.031757 ± 0.000001	0.031607 ± 0.000107	0.460169 ± 0.000001	0.458375 ± 0.004236
17	Q0.500_0.00_0.50	0.050577 ± 0.000012	0.049510 ± 0.000268	0.778577 ± 0.000018	0.778307 ± 0.004860
18	Q0.500_−0.80_0.20	0.038377 ± 0.000001	0.037656 ± 0.000195	0.638918 ± 0.000018	0.638885 ± 0.004488
19	Q0.500_0.80_−0.20	0.039610 ± 0.000013	0.039003 ± 0.000172	0.606313 ± 0.000022	0.605347 ± 0.004643
20	Q0.500_−0.80_−0.40	0.030257 ± 0.000001	0.029824 ± 0.000142	0.441854 ± 0.000004	0.441744 ± 0.003427
21	Q0.500_0.80_0.40	0.054693 ± 0.000002	0.053274 ± 0.000363	0.790499 ± 0.000012	0.791070 ± 0.005010
22	Q0.500_−0.80_−0.80	0.026965 ± 0.000001	0.026574 ± 0.000175	0.305299 ± 0.000000	0.304648 ± 0.004239
23	Q0.500_−0.80_0.80	0.054259 ± 0.000001	0.052322 ± 0.000535	0.823813 ± 0.000016	0.825549 ± 0.005449
24	Q0.500_0.80_−0.80	0.031687 ± 0.000001	0.031281 ± 0.000219	0.410368 ± 0.000001	0.408069 ± 0.005900
25	Q0.500_0.80_0.80	0.075669 ± 0.000021	0.071617 ± 0.001144	0.902719 ± 0.000354	0.906457 ± 0.008499
26	Q0.333_0.00_−0.67	0.021506 ± 0.000006	0.021379 ± 0.000114	0.240088 ± 0.000006	0.239368 ± 0.003257
27	Q0.333_0.00_0.67	0.045862 ± 0.000010	0.044039 ± 0.000455	0.823471 ± 0.000025	0.825458 ± 0.005127
28	Q0.333_−0.80_0.80	0.047937 ± 0.000014	0.046294 ± 0.000398	0.855825 ± 0.000188	0.857221 ± 0.004083
29	Q0.333_0.80_−0.80	0.022026 ± 0.000004	0.021768 ± 0.000115	0.206316 ± 0.000002	0.205397 ± 0.003613
30	Q0.250_0.00_−0.75	0.016007 ± 0.000001	0.015923 ± 0.000101	0.067207 ± 0.000000	0.066201 ± 0.002989
31	Q0.250_0.00_0.75	0.041023 ± 0.000005	0.038639 ± 0.000449	0.852368 ± 0.000083	0.855422 ± 0.004317
32	Q0.250_0.80_−0.80	0.016470 ± 0.000000	0.016191 ± 0.000100	0.057516 ± 0.000001	0.057117 ± 0.002698
33	Q0.200_0.00_−0.80	0.012631 ± 0.000007	0.012556 ± 0.000091	-0.067330 ± 0.000001	-0.067585 ± 0.002660
34	Q0.200_0.00_0.80	0.036968 ± 0.000044	0.034071 ± 0.000500	0.872432 ± 0.000480	0.876983 ± 0.004144
35	Q0.167_0.00_−0.83	0.010495 ± 0.000004	0.010396 ± 0.000067	-0.172301 ± 0.000003	-0.172286 ± 0.001438
36	Q0.167_0.00_0.83	0.033350 ± 0.000003	0.030324 ± 0.000367	0.888377 ± 0.000166	0.893634 ± 0.003402
37	Q0.100_0.00_0.00	0.0044 ± 0.0001		0.261 ± 0.002	

$$\tilde{\xi} = a + b\tilde{S}_{\parallel} + c\delta m\tilde{\Delta}_{\parallel}, \tag{18}$$

where we have added a leading power of η^2 to the expansion. The issue of the leading power of η for the recoil was discussed in the context of the off-plane recoils in Refs. [12,38], where the possibility of a leading η^3 versus η^2 was studied with full numerical simulations. Further study of recoils in the small mass ratio perturbative regime [61] led to the conclusion that the terms of the recoil linear in the spin should scale as η^2, and post-Newtonian expansions including quadratic terms in the spin also show a leading η^2 behavior [43] (again, for low eccentricity, in-plane orbits).

Finally, we tested the leading η^2 dependence in Eq. (17) by allowing the power of η to be free. Interestingly, we do not find $p = 2$, but rather we find that the minimum in the fit is quite shallow, with similar results for the interval $1.5 \leq p \leq 2.5$ (the minimum is at $p \sim 2.29$). Since $p = 2$ gives the correct particle limit behavior for quasicircular orbits (at least at moderate mass ratios; however, see Refs. [62,63] for a discussion on resonance recoil which scales as $\eta^{1.5}$), we enforce $p = 2$ for the fits presented in Table VI.

We note that a factor of η^p in the coefficients is not independent of the expansion proposed in Refs. [8] and [59] since $4\eta = 1 - \delta m^2$ and this allows us to recast all powers of η into the original form of the expansion.

TABLE VI. Table of fitting parameters for recoil, mass, and spin formulas.

H	$7367.250029 \pm 66.122336$	M0	0.951507 ± 0.000030	L0	0.686710 ± 0.000039
H2a	-1.626094 ± 0.053888	K1	-0.051379 ± 0.000193	L1	0.613247 ± 0.000168
H2b	-0.578177 ± 0.055790	K2a	-0.004804 ± 0.000514	L2a	-0.145427 ± 0.000473
H3a	-0.717370 ± 0.077605	K2b	-0.054522 ± 0.000690	L2b	-0.115689 ± 0.000761
H3b	-2.244229 ± 0.137982	K2c	-0.000022 ± 0.000010	L2c	-0.005254 ± 0.000332
H3c	-1.221517 ± 0.176699	K2d	1.995246 ± 0.000497	L2d	0.801838 ± 0.000514
H3d	-0.002325 ± 0.021612	K3a	0.007064 ± 0.002680	L3a	-0.073839 ± 0.002986
H3e	-1.064708 ± 0.133021	K3b	-0.017599 ± 0.001678	L3b	0.004759 ± 0.001374
H4a	-0.579599 ± 0.297351	K3c	-0.119175 ± 0.001054	L3c	-0.078377 ± 0.000911
H4b	-0.455986 ± 0.302432	K3d	0.025000 ± 0.001951	L3d	1.585809 ± 0.001777
H4c	0.010963 ± 0.174289	K4a	-0.068981 ± 0.004251	L4a	-0.003050 ± 0.001910
H4d	1.542924 ± 0.274459	K4b	-0.011383 ± 0.001709	L4b	-0.002968 ± 0.001431
H4e	-4.735367 ± 0.430869	K4c	-0.002284 ± 0.000192	L4c	0.004364 ± 0.000532
H4f	-0.284062 ± 0.174087	K4d	-0.165658 ± 0.003100	L4d	-0.047204 ± 0.003250
a	2.611988 ± 0.028327	K4e	0.019403 ± 0.003220	L4e	-0.053099 ± 0.003682
b	1.383778 ± 0.092915	K4f	2.980990 ± 0.001197	L4f	0.953458 ± 0.001210
c	0.549758 ± 0.113300	K4g	0.020250 ± 0.002524	L4g	-0.067998 ± 0.002369
		K4h	-0.004091 ± 0.002057	L4h	0.001629 ± 0.000980
		K4i	0.078441 ± 0.003263	L4i	-0.066693 ± 0.003289

The 17 constants in Eqs. (17) and (18), 19 constants in Eq. (14), and 19 constants in Eq. (16) were obtained by a least-squares fit to the results of our 36 simulations and, in the case of the fits of the final mass and spin, an additional 38 SXS runs [64] and a $q = 1:10$ simulation. Note that, as explained above, we allow $v_\perp$ to be positive and negative and thereby allow $\tilde{\xi}$ to be continuous (see Fig. 7).

The results of the recoil velocity fit and residuals to the entire set of 36 runs is shown in Fig. 5. We observe that the residuals are below 7 km s^{-1}.

In order to assess the accuracy of our formula, we compare its predictions for 8 independent runs from the group at AEI reported in Ref. [65] and 16 from the SXS Collaboration in Ref. [64]. The results are shown in Fig. 6. We observe that while the residuals of our runs and those of AEI are similar and relatively small (i.e., within 10 km s^{-1}), the residuals with respect to the SXS runs are roughly 3 times larger. We note that while in this paper (and Ref. [65]) recoils are computed using the radiated linear momentum, the SXS catalog reports coordinate velocities. Coordinate velocities are gauge dependent and therefore only an approximation to the true recoil.

Note that while we use the recoils of Ref. [65] as an independent test of our fitting formula, the recoil formula proposed in [65] [Eq. (42) there] does not respect the symmetry of exchange of black-hole labels $1 \leftrightarrow 2$; hence, we would expect it to be less accurate outside of the region of parameter space used to generate that fit.

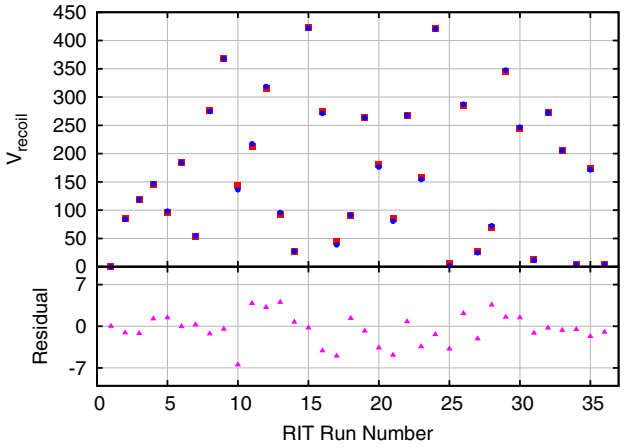

FIG. 5 (color online). Fit and residuals to 36 RIT data (see Table IV) with a root mean square deviation, RMS = 2.5 km s^{-1}.

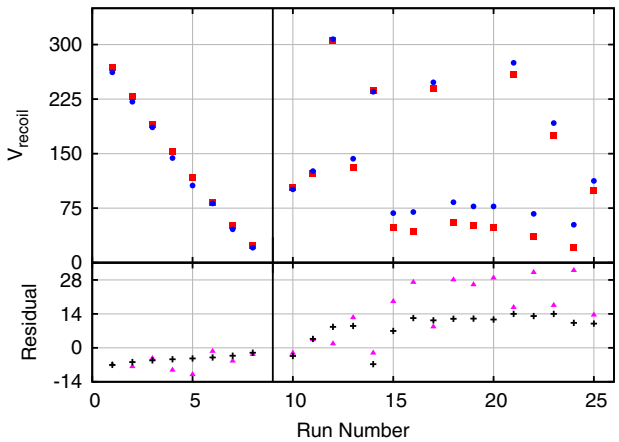

FIG. 6 (color online). Recoil fit, fit residuals (diamonds), and variation in the fit prediction (cross) for the 8 AEI (RMS = 6.8 km s^{-1}) simulations and 16 SXS (RMS = 20 km s^{-1}) simulations. The variations in the fit prediction have been adjusted to take into account the truncation error as given in Appendix B.

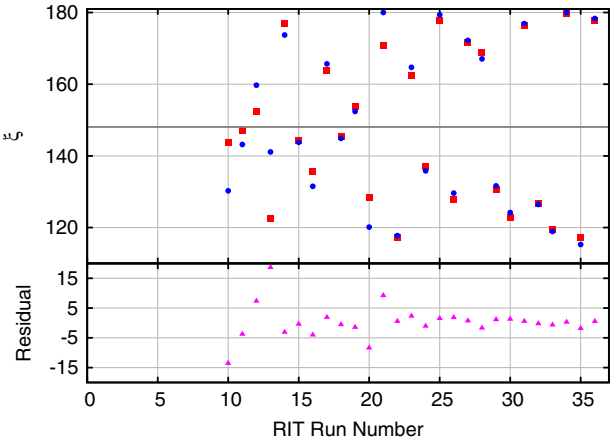

FIG. 7 (color online). The angle $\tilde{\xi}$ as defined in Eq. (18), computed from the measured magnitude of the recoil (circles), compared to the fitted formula (squares). The angle is not defined for the (first) 9 equal mass runs in Table IV. The average of $\tilde{\xi} \sim 148°$ (gray line) is near the previously measured value of $\tilde{\xi} \sim 145°$, but the new spin-dependent formula for $\tilde{\xi}$ significantly reduces the residuals.

Interestingly, by allowing $v_\perp$ in Eq. (12) to take on positive and negative values, the angle $\tilde{\xi}$ can be restricted to the interval $90° \leq \tilde{\xi} \leq 180°$, and its average value, as shown in Fig. 7, is $\tilde{\xi} \sim 148°$, which is very close to the estimate $\tilde{\xi} \sim 145°$ in Ref. [39]. Note that the dispersion is quite large though. As part of our fitting of the recoil, we must simultaneously fit $\tilde{\xi}$ to Eq. (18). Interestingly, the choice of coefficients in Eq. (18) that optimizes the fit is close to $c/b = 3/7$. This ratio is significant because the effective spin defined in Ref. [66] is given by $\vec{S}_{\rm effective} = \vec{S} + \frac{3}{7}\vec{\Delta}\delta m$. Thus, it appears that the functional form of $\tilde{\xi}$ that minimizes the residuals is essentially a linear function in the effective spin.

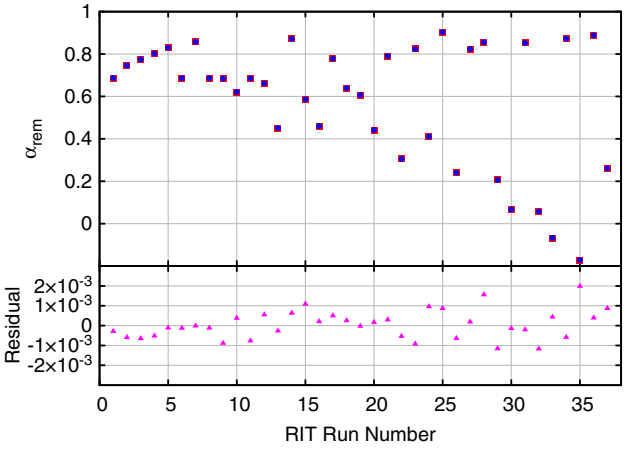

FIG. 8 (color online). Fit to the remnant spin using RIT + SXS data and residuals of RIT runs as labeled by run number (see Table V). RMS $= 7.16 \times 10^{-4}$.

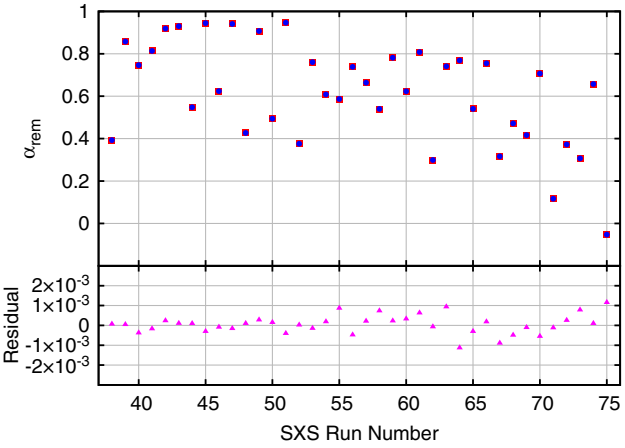

FIG. 9 (color online). Fit to the remnant spin using RIT + SXS data residuals for the SXS data. RMS $= 4.73 \times 10^{-4}$.

The fitted values of all coefficients in Eqs. (17) and (18), as well as the uncertainties in these values, are given in Table VI. We estimate the errors in the fitting parameters by adding Gaussian distributed random noise to the fitting function. Each data point is given a different random number, and the width of the Gaussian is determined by the estimated error in that data, as given in Table IV. By performing the fit 50,000 times, each with a different set of noise, a distribution in the fitting parameters is found. The standard deviation of these distributions is recorded as the error in the fitting parameter in Table VI. The truncation error is not included in the determination of the errors in the parameters because we only have this error for the simulations given in Appendix B. If we assume that all the simulations have roughly the same level of truncation error as the simulations in Appendix B, the errors in the fitting parameters will increase by a factor of between 2 and 3.

We use a similar procedure to fit the final remnant mass and spin to Eqs. (14) and (16). Here, however, we add the data from the SXS catalog [64] (which include results from highly spinning BHBs) into our fits, as well as results from a nonspinning binary with mass ratio $q = 1/10$ from Refs. [67,68]. The resulting fitting parameters are given in

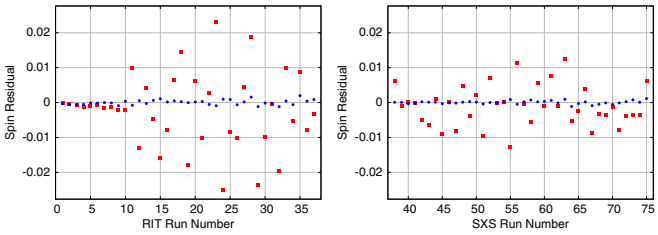

FIG. 10 (color online). A comparison of the residuals from our spin fit and the AEI fit for the RIT data (left panel) and SXS data (right panel). Residuals from our formula are denoted by (blue) circles, and residuals from the AEI formula are denoted by (red) squares.

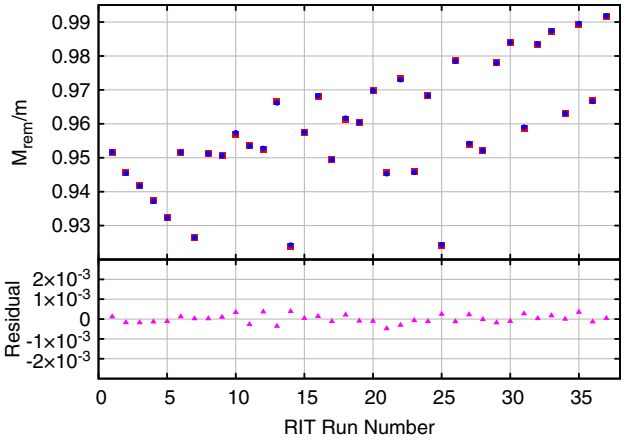

FIG. 11 (color online). Predicted and measured remnant mass for RIT data versus run number. RMS $= 2.07 \times 10^{-4}$.

Table VI. The data, fit, and residuals for the remnant spins are shown in Figs. 8 and 9. The residuals are below 6×10^{-4}.

We can compare the residuals of our fit with other fitting formulas in the literature, for instance, for the final spin of the merged black hole given in Ref. [69] (we denote this fit by AEI). The results are shown in Fig. 10 for the current data (RIT) and the SXS data. We observe a clear improvement of our fitting formula (16), with over an order of magnitude reduction in the residuals. Note that here we are comparing the error in the predictions of the AEI formula with our fit residuals rather than errors in predictions of the AEI and RIT fits to independent data.

We see that our fitting formula for the final remnant spin is remarkably accurate over a wide range of mass ratios. In addition, we constructed the formula such that it gives the correct small-mass limit behavior. We thus expect that our formula will be reasonably accurate for all mass ratios, at least for moderate spins ($\alpha \leq 0.9$).

A similar analysis for the final remnant mass is shown in Figs. 11, 12, and 13. Once again, we used the SXS data in

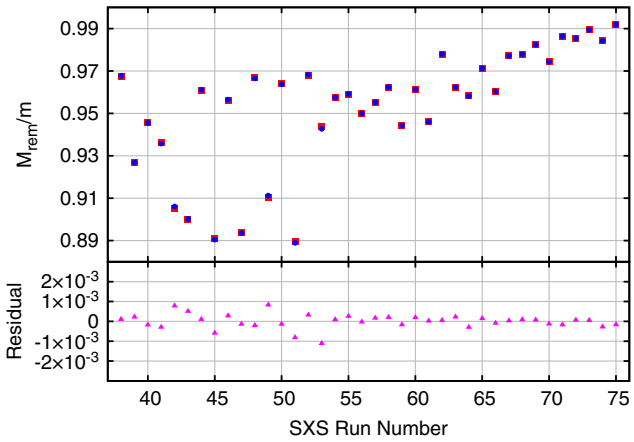

FIG. 12 (color online). Predicted and measured remnant mass for the SXS data. RMS $= 3.56 \times 10^{-4}$.

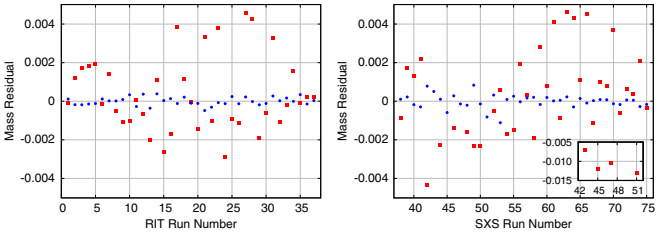

FIG. 13 (color online). Residuals for our mass fit (small blue circles) to the RIT (left panel) and SXS data (right panel) compared to the AEI fitting formula (large red squares).

generating our fits. Here we see residuals of order 3×10^{-4} for our new formula and residuals several times larger for the AEI formula [70].

An interesting consequence of the form of the recoil velocity (17) is that, for certain combinations of the spins and the mass ratio, the total magnitude can be very small. In Fig. 14 we plot the values of α_2 and q that lead to small recoils for a given α_1. Apart from the zero recoil imposed by symmetry, i.e., $q \to 0$ and $q = 1, \alpha_1 = \alpha_2$, there appear to be two branches that lead to vanishing recoils. One branch spans all mass ratios with $0.6 \lesssim \alpha_2 \lesssim 0.75$, and the other branch only spans the smaller mass ratio regime $q \lesssim 0.4$ and larger spins $0.74 \lesssim \alpha_2 \leq 1$.

Interestingly, the vanishing of the recoil velocity does not arise from any symmetry, but rather from a cancellation of processes that involve a wobbling of the center of mass as the BHB slowly inspirals, the recoil generated during the rapid plunge, and the post-merger antikick [71], which is generated during the ringdown phase. All of these three stages combine to produce a nonmoving final BH, but in the process, the BH is displaced from the original center of mass of the binary. In Fig. 15 we provide an explicit example for run #25 Q0.500_0.80_0.80 of a near-zero final recoil.

It is interesting to recall here the zero-recoil superkicks seen in [6,42]. In that case the bobbing of the BHs up and

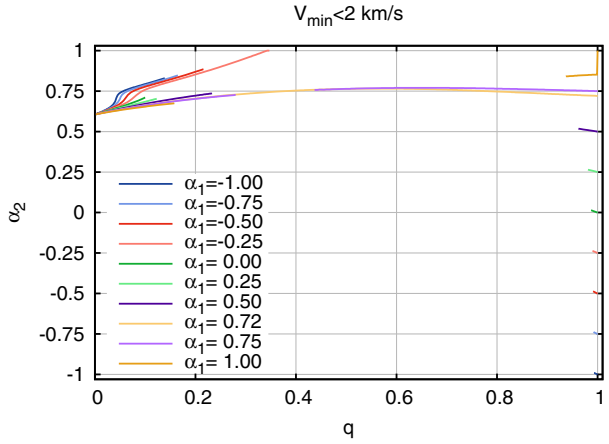

FIG. 14 (color online). The BHB configurations that lead to a final remnant black hole with zero recoil. Additional zero recoils exist for $q = 0$ and for $q = 1$ with $\alpha_1 = \alpha_2$.

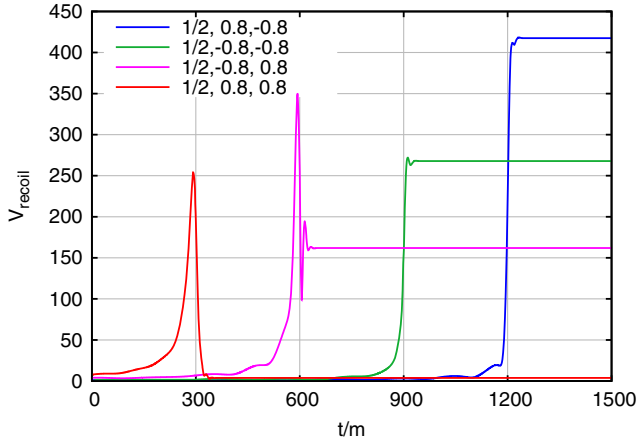

FIG. 15 (color online). The radiated linear momentum for the Q0.500_0.80_0.80 configuration (red line). We observe the wobbling from the inspiral, a sudden rise to above 250 km s^{-1} due to the merger, and the final antikick from the ringdown phase which reduces the final velocity of the remnant to 2 km s^{-1}. For comparison we also show the Q0.500_ $\pm$ 0.80_ $\pm$ 0.80 configurations to see the different effects of the superposition of spin (signs) and unequal mass components of the recoil.

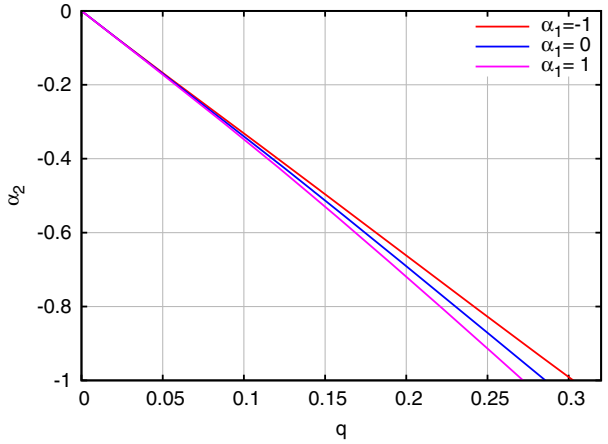

FIG. 16 (color online). The BHB configurations that lead to a final Schwarzschild black hole. We note that the spin of the small black hole has little influence on the values of the mass ratio and spin of the large black hole that lead to a vanishing final spin.

down can be tuned by choosing the azimuthal orientation of the spin such that the merger occurs when the bobbing velocity is instantaneously zero, which leads to a vanishing recoil.

In Fig. 15 we show the velocity of the center of mass versus time for the four possible combinations of signs of the spins for a $q = 1/2$ binary with spin magnitudes $\alpha_i = 0.8$ (Q0.500_ $\pm$ 0.80_ $\pm$ 0.80). The UD configuration Q0.500_0.80_ $-$ 0.80 recoils at 420 km s^{-1}, while the DD configuration recoils at a more modest 267 km s^{-1}. Reversing the spin directions for both BHs leads to a DU configuration that recoils at 154 km s^{-1}. Finally, a UU configuration recoils at a very small 2 km s^{-1}. Notably, the recoil of the DU configuration agrees with the purely unequal mass recoil $v_m(q = 1/2)$, and the difference between the recoil velocities of the UD and DU configurations, as well as the differences in the recoil between the DD and UU configurations, is around 266 km s^{-1}.

It is also interesting to see which configurations lead to a remnant with vanishing spin [as was done in Ref. [72], Fig. 4(a)]. Our results are shown in Fig. 16. They show that in order to have a final Schwarzschild black hole, the larger hole must be counteraligned with the orbital angular momentum and the smaller hole must bear a mass ratio of less than 0.3. This small mass ratio also explains the relatively weak dependence on the spin of the secondary black hole.

In the equal-mass regime, Eq. (14) predicts a maximum amount of radiated energy of $M_{\rm rem}^{\rm max}/m = 0.88693 \pm 0.00027$, i.e., a maximum radiated energy of 11.3%, and Eq. (16) predicts a maximum remnant spin of $\alpha_{\rm rem}^{\rm max} = 0.95166 \pm 0.00027$, both of which are close to the predictions of Ref. [73] (11.397% and 0.951383, respectively). The differences between our extrapolation and those of Ref. [73] are likely due to higher-order terms not included in Eqs. (14) and (16).

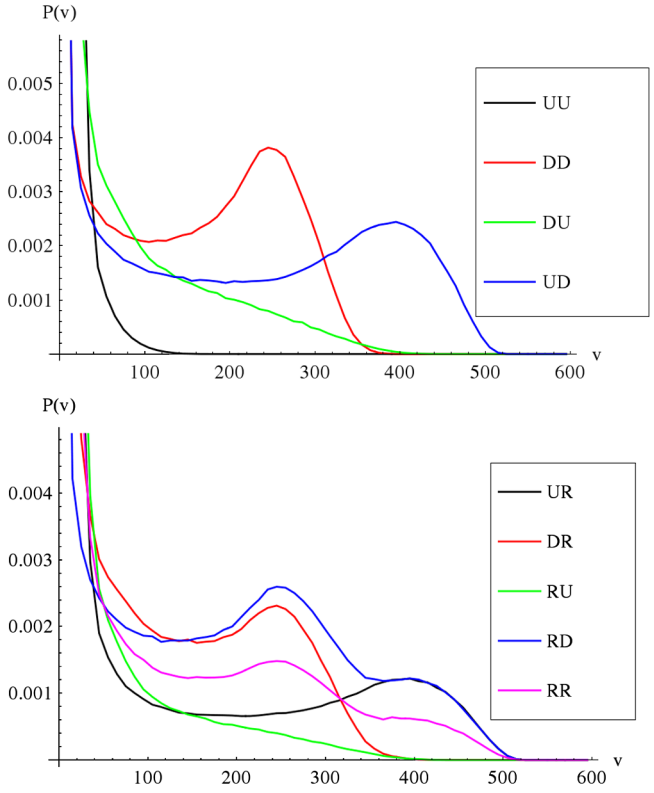

FIG. 17 (color online). The probability $P(v)$ of the remnant BH recoiling with speed v assuming a distribution of progenitor binaries with spin magnitude given by the cold accretion model of [7] and mass ratio distribution given by [74], and assuming the first (smaller) BH or second (larger) BH is always aligned (U), always counteraligned (D), or randomly (R) distributed with equal probability of being aligned or counteraligned.

In the above analysis we truncated our fits at fourth order. In Appendix B we compare these results with third-order fits.

V. STATISTICAL DISTRIBUTIONS

In order to visualize the consequences of Eqs. (14), (16), (17), and (18), we study the distributions of recoils and remnant masses and spins from BHBs where the individual BH spins are either aligned or counteraligned with the orbital angular momentum. We study nine families of distributions of progenitors: both BH spins aligned with the orbital angular momentum, both counteraligned, two families where one BH is aligned and the other counteraligned, four families where one BH spin direction is chosen randomly (aligned or counteraligned) and the other direction is fixed, and one family where both BH orientations are chosen randomly. In all cases the spin magnitudes are chosen from the cold accretion distribution in [7], which is represented by $P(\alpha) = (1-\alpha)^{b-1}\alpha^{a-1}$ (where $a = 5.935$ and $b = 1.856$), and the mass ratio distribution from [74–76], which is given by $P(q) \propto q^{-0.3}(1-q)$. In Figs. 17, 18, and 19 we show the probabilities for a remnant recoiling with speed v, having mass $M_{\rm rem}$ and spin $\alpha_{\rm rem}$.

There are several interesting things to note from Fig. 17. First, the probability for large recoils is much larger for the UD family of configurations than for any of the other (nonrandom) configurations. The UR and RD (here R denotes that the spin orientation is chosen randomly) families both show the same probabilities at high velocities. The reason for this is that high velocities can only come from a UD-type configuration. Both the UR and RD families have a 50% probability for a given configuration to be UD.

From Fig. 18 we see that the UU families show significant probabilities for smaller remnant mass. Small remnant masses occur for near-equal-mass UU systems, as this maximizes the radiated energy. The UR, RU, and RR

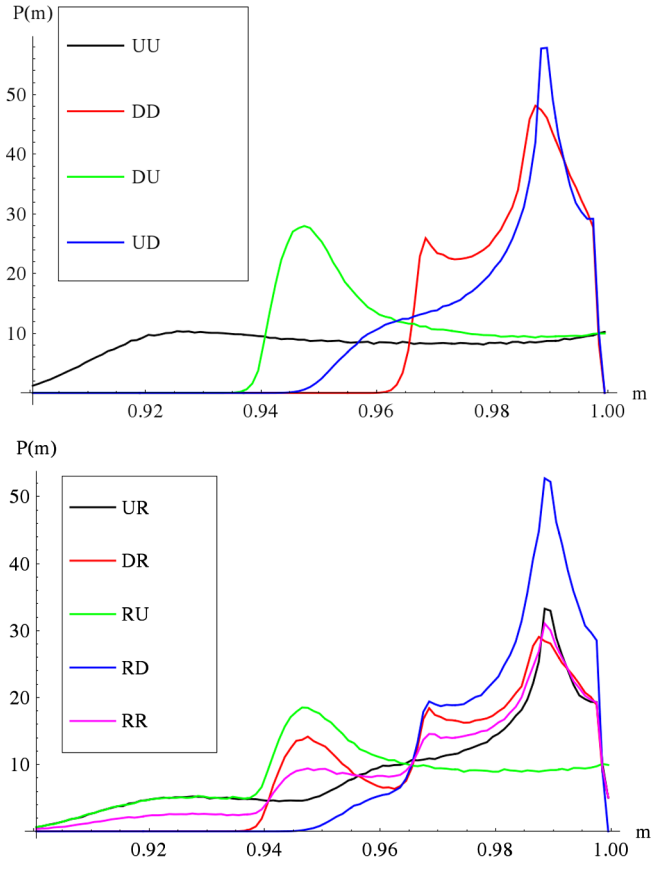

FIG. 18 (color online). The probability $P(m)$ of the remnant BH having mass m (in units of the initial mass $M_1 + M_2$) assuming a distribution of progenitor binaries with spin magnitude given by the cold accretion model of [7] and mass ratio distribution given by [74] and assuming the first (smaller) BH or second (larger) BH is always aligned (U), always counteraligned (D), or randomly (R) distributed with equal probability of being aligned or counteraligned.

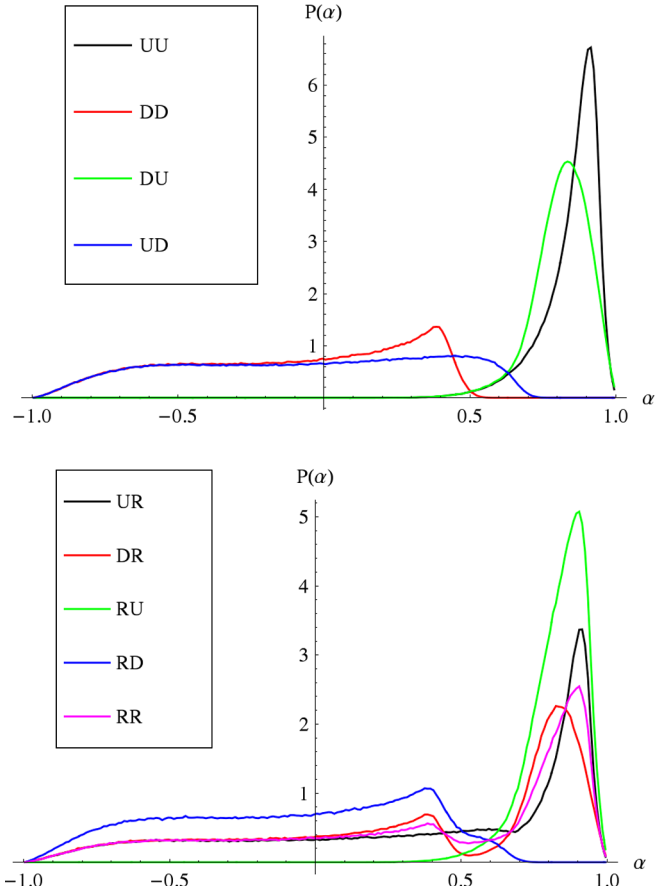

FIG. 19 (color online). The probability $P(\alpha)$ of the remnant BH having dimensionless spin α assuming a distribution of progenitor binaries with spin magnitude given by the cold accretion model of [7] and mass ratio distribution given by [74] and assuming the first (smaller) BH or second (larger) BH is always aligned (U), always counteraligned (D), or randomly (R) distributed with equal probability of being aligned or counteraligned.

families show a similar tail at smaller remnant masses. The UR and RU configurations have a 50% probability of being UU, and the RR configurations have a 25% probability of being UU. Hence the $P(m)$ for the RR configurations is half the value of $P(m)$ for the UR and RU families.

Finally, in Fig. 19 we see that the probability for a final remnant spin counteraligned with the binary's orbital angular momentum is nearly equal for the DD and UD families. The reason is that this can only happen in the small mass ratio regime with a counteraligned larger BH. The UR, DR, RR configurations show similar tails near $\alpha = -1$. Again, these configurations have a 50% probability of being an XD configuration (here X just means that the orientation of the smaller BH is unimportant).

In Fig. 20 we show the integrated probability $\Pi(v)$ for a recoil v or larger, where

$$\Pi(v) = \int_v^\infty P(\nu) d\nu,$$

and $P(\nu)$ is the probability for a recoil with speed $\nu < v < \nu + d\nu$.

We can thus consider a scenario where coherent accretion aligned the smaller BH spin but left the spin of the larger BH either aligned or counteraligned (with equal probability). For such a UR configuration, we find that the probability for $V > 250$ km s^{-1} is nearly 23%, while the probability for $V > 400$ km s^{-1} is 8.4%. If we assume that both BHs are equally likely to be aligned or counteraligned, the probabilities reduce to 19% and 4.2%, respectively. While these recoil velocities are enough to expel the merged BHs from galaxies similar to the Milky Way, they are not enough for the BHs to escape from much larger galaxies. Nevertheless, these recoils can still produce observational effects such as displacement of the central BH from the galactic core or a disturbance in the velocity field of nearby stars [4]. We also note that these recoil velocity probabilities represent a lower bound for large recoils since we assumed exact alignment (or counteralignment) of the spins with the orbital angular momentum, and components of the spin on the orbital plane can lead to very large recoils [6,8] even for relatively small misalignment angles, i.e., a few degrees.

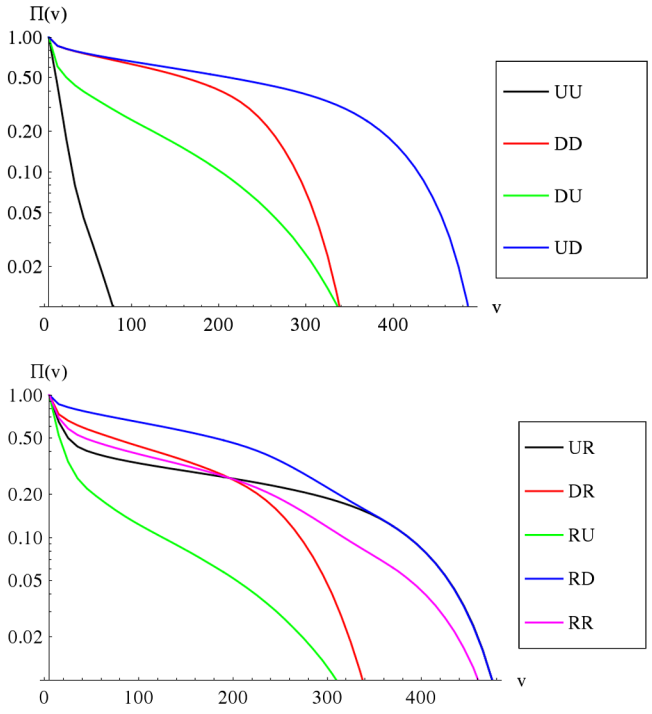

FIG. 20 (color online). The integrated probability $\Pi(v)$ of the remnant BH recoiling with speed v or larger assuming a distribution of progenitor binaries with spin magnitude given by the cold accretion model of [7] and mass ratio distribution given by [74] and assuming the first (smaller) BH or second (larger) BH is always aligned (U), always counteraligned (D), or randomly (R) distributed with equal probability of being aligned or counteraligned.

VI. CONCLUSIONS AND DISCUSSION

We studied the merger remnant of nonprecessing BHBs as a function of the individual BH spins and mass ratio. As accretion [27,77] and resonances [33,34] align spins with the orbital angular momentum, this represents an important subcase of the more general, seven-dimensional parameter space of binaries, which includes arbitrary orientation of the spins. The study performed here allowed us to use the unified phenomenological description of a BHB merger developed in [8,59] to model the recoil (17), remnant mass (14), and spin (16), with expected accuracies to within 3%, 1%, and 1% relative errors, respectively.

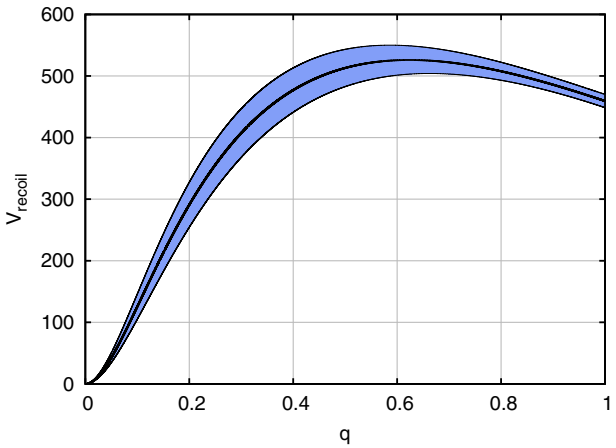

FIG. 21 (color online). The recoil velocity for the UD configuration with the small black hole spin aligned with the orbital angular momentum and the large hole spin counteraligned as a function of the mass ratio as predicted by Eq. (17). The maximum recoil of 526 ± 23 km s^{-1} is reached at $q = 0.6235 \pm 0.038$, with maximally spinning holes, $\alpha_1 = 1.0$, $\alpha_2 = -1.0$. The shaded area represents the estimated errors.

TABLE VII. Case studies A and B with BHs at two different initial separations, with two sets of parameters from estimated quasicircular orbits.

Configuration	x_1/m	x_2/m	P/m	m_1^p/m	m_2^p/m	S_1/m^2	S_2/m^2	m_1^H/m	m_2^H/m	$M_{\rm ADM}/m$	a_1/m_1^H	a_2/m_2^H
A_DU0.8	−4.9832	4.5267	0.09905	0.30178	0.30168	−0.2	0.2	0.5	0.5	0.98951	−0.8	0.8
B_DU0.8	−4.5465	4.4303	0.10557	0.30377	0.30366	−0.20465	0.20465	0.5053	0.5053	1	−0.8	0.8

We found that the spin contribution to the recoil can add to, or subtract from, the component of the recoil due to unequal masses, with (partial) cancellation occurring when the larger BH spin is aligned with the orbital angular momentum. On the other hand, when the larger BH spin is counteraligned, the two components of the recoil add, leading to larger recoils at intermediate mass ratios. We find that the maximum recoil occurs for $q \sim 0.62$.

Also note that the new maximum of the recoil (see Fig. 21) represents a modest increase in the maximum value itself (nearly 17%). However, just like for the case of the hangup kicks [6], the most important effect is that the volume of parameter space leading to large recoils is much larger; i.e., the UD configurations have ($V_{\rm recoil} > 200\ {\rm km\,s^{-1}}$) with a 52% probability.

Another similarity with the hangup kick effect is the need to incorporate terms beyond linear in the spins (and mass ratio) to accurately model the final recoil (and mass and spin). This underlines the inherently nonlinear nature of general relativity, in particular, when modeling the highly dynamical regime of BHB mergers.

This provides the opportunity for an important test of general relativity in its strong field realm. Searches for observational effects from recoiling black holes are well underway. This includes searches for large differential red or blue shifts from active galactic nuclei (AGN) (see [31] for a review), and distortions in the dynamics of the core of galaxies (see [32] for the latest observation that the lack of black holes in bright cluster galaxies might be the result of large kicks).

We finally note that the use of gravitational waveforms from aligned and antialigned spins proves to be of great help for detection algorithms [78] used by laser interferometer observatories. Our models for the final mass and spin from the merger of two black holes can be used to produce more accurate semianalytic models of such waveform templates, which may also be used for parameter estimation.

ACKNOWLEDGMENTS

The authors gratefully acknowledge the NSF for financial support from Grants No. PHY-1305730, No. PHY-1212426, No. PHY-1229173, No. AST-1028087, No. PHY-0969855, No. OCI-0832606, and No. DRL-1136221. Computational resources were provided by XSEDE allocation TG-PHY060027N, and by NewHorizons and BlueSky Clusters at Rochester Institute of Technology, which were supported by NSF Grants No. PHY-0722703, No. DMS-0820923, No. AST-1028087, and No. PHY-1229173.

APPENDIX A: ANALYSIS OF THE SOURCES OF ERRORS AND ROBUSTNESS OF REMNANT PROPERTIES IN THE BHB SIMULATIONS

In order to assess the robustness of our results with respect to the different sources of errors and the various approximations that we use in our simulations, we study in

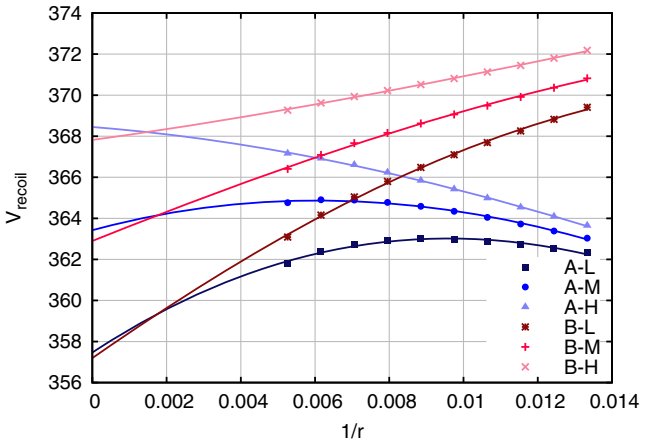

FIG. 22 (color online). The recoil velocity as computed at a given extraction radius: $75M$–$190M$ and extrapolations to infinity. The different curves correspond to the two initial separations labeled as A and B and as a function of resolution (low, medium, high) refined by a global factor 1.2. A quadratic least-squares fit is shown for each.

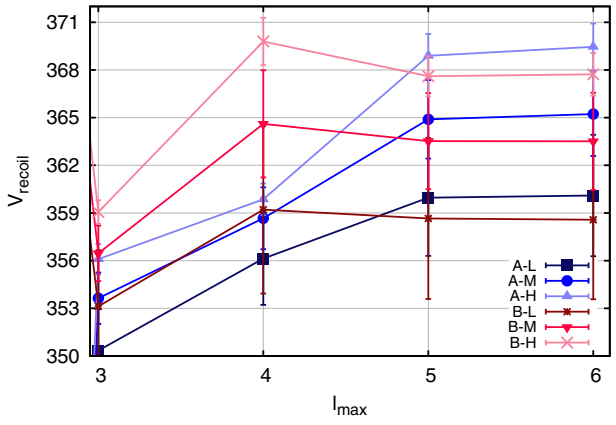

FIG. 23 (color online). The dependence of the computed recoil velocity on the number of ℓ modes used to construct the radiated linear momentum. Here all modes with $\ell \leq \ell_{\rm max}$ were used, and we show the recoil for the A and B configurations for the low, medium, and high resolution runs.

detail an equal-mass BHB in a UD configuration (with spins $\alpha = 0.8$) starting from two different initial separations. We vary the resolutions, grid structure, waveform extraction radii, and the number of ℓ modes used in the construction of the radiated linear momentum. The initial data parameters for the two configurations, denoted here by A and B, are given in Table VII.

Case A represents a prototypical configuration of the runs in this paper, while case B was first studied in Ref. [59], where we also performed a convergence study of that configuration. In this work we use a grid structure with between 9 and 11 levels of refinement, depending on mass ratio and spin. For all new simulations, the outer boundary was placed at 400M with a resolution of $4M$ on the coarsest level and a resolution of $1M$ in the wave zone. The finest level around each BH was as wide as twice the diameter of the relaxed horizon (the number of points across each horizon was between 28 and 60). In addition, for the highly spinning horizons, we added another level inside the horizon of width roughly half of the horizon diameter. We also performed similar runs but with resolutions in the wave zone of $M/0.88$ and $M/1.2$.

Since in the current work we use a different refinement level grid structure than in Ref. [59], we also perform a new set of convergence simulations for case B using the newer grid structures.

Aside from truncation errors due to finite resolution, the simulation results will depend on the extraction radii. Hence we also consider different extraction radii and

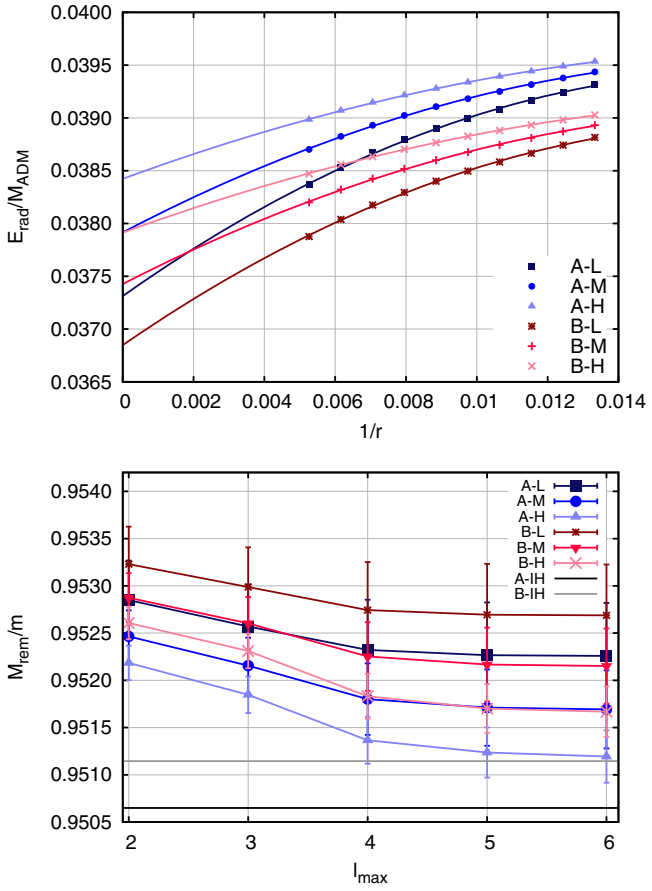

FIG. 24 (color online). Top panel: The radiated energy as computed at a given extraction radius: $75M$–$190M$ and extrapolations to infinity. The different curves correspond to the two initial separations labeled as A and B and as a function of resolution (low, medium, high) refined by a global factor 1.2. A quadratic least-squares fit is shown for each. Bottom panel: The dependence of the computed radiated energy on the number of ℓ modes used to construct it. Here all modes with $\ell \leq \ell_{\max}$ were used. The black and gray lines labeled with "IH" are the associated final mass calculated from the BH horizon. On this scale, all resolutions are on top of one another, so only one line is shown.

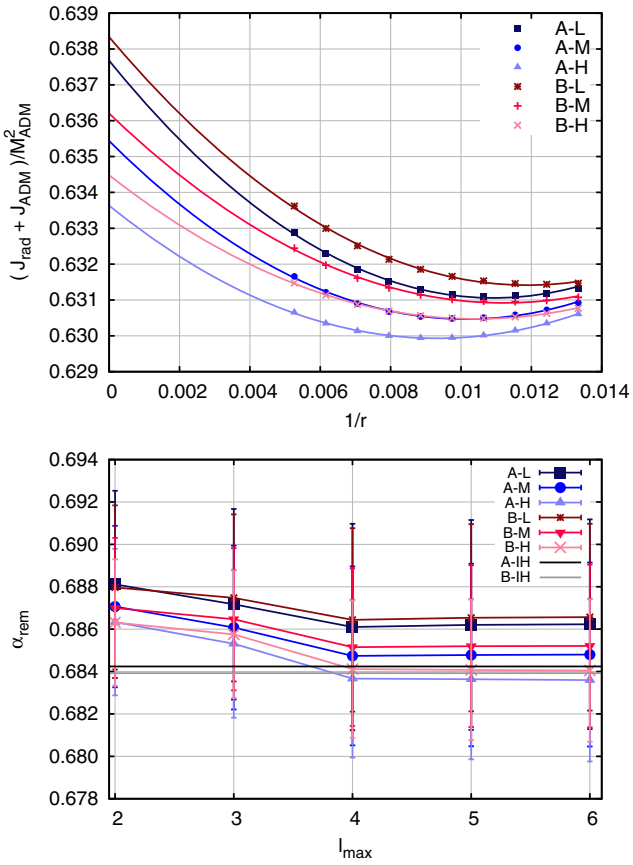

FIG. 25 (color online). Top panel: The radiated angular momentum as computed at a given extraction radius: $75M$–$190M$ and extrapolations to infinity. The different curves correspond to the two initial separations labeled as A and B and as a function of resolution (low, medium, high) refined by a global factor 1.2. A quadratic least-squares fit is shown for each. Bottom panel: The dependence of the computed radiated angular momentum on the number of ℓ modes used to construct it. Here all modes with $\ell \leq \ell_{\max}$ were used. The black and gray lines labeled with "IH" are the associated final spin calculated from the BH horizon. On this scale, all resolutions are on top of one another, so only one line is shown.

extrapolations to null infinity. While the location of the observers in the set of runs in Ref. [59] was restricted to the $R_{\rm obs}/M = 60$–100 range, in the runs of this paper we extended this to $R_{\rm obs}/M = 190$ and, in addition, located the extraction radii equidistant in $1/R$, with $R_{\rm obs}/M =$ 75, 80.4, 86.7, 94.0, 102.6, 113.0, 125.7, 141.7, 162.3, 190.0. The results of such studies are displayed in Fig. 22.

Interestingly, we see that while the measured recoils from the A and B simulations differ by ~ 30 km s^{-1} at lower resolution and smaller radii, they approach each other as both the resolution and extraction radii increase. The difference in the extrapolated recoil for the highest resolution A and B configurations is smaller than 10 km s^{-1}.

In Fig. 23 we show the recoil extrapolated to infinity versus the number of ℓ modes. Interestingly, for the B configuration, using all modes up through $\ell = 4$ appears to be sufficient, while for the A configuration, there is a noticeable change in the recoil when adding the $\ell = 5$ modes.

Based on the results in Figs. 22 and 23, we used the medium resolution grid structure (i.e., A-M in the figures) and summed all modes up through $\ell = 6$ when calculating the recoils given in the tables and figures of this work. We

TABLE VIII. Fits of the remnant mass, spin, and recoil to the form $X = X_\infty + A(1/h)^n$, as well as measures of the truncation and extrapolation errors in these quantities for the A configurations. In the table below, 1st and 2nd denote quantities obtained at $r = \infty$ using first-order and second-order extrapolations, respectively, while the subscripts rad and IH refer to radiative and isolated horizon measures, respectively. Finally, med refers to a quantity measured using the medium resolution run, and ∞ denotes a quantity Richardson extrapolated to infinite resolution (i.e., X_∞). Isolated horizon measures are the most accurate, and for radiative quantities, radial extrapolation errors are of the same magnitude as truncation errors. Finally, the difference *Radiative v IH* measures how different the radiative and IH quantities are, *Extrapolation error* measures the error in radial extrapolation, and *Truncation error* measures the truncation error. Note that S is given in units of M^2 and V is in units of km s^{-1}.

Variable	X_∞	A	n
$M_{\rm rad}^{\rm 1st}$	0.950512	2493.83	−3.20426
$M_{\rm rad}^{\rm 2nd}$	0.950598	2405.2	−3.13343
$M_{\rm IH}$	0.950649	-7.21411×10^{15}	−10.7552[a]
Radiative v IH	$M_{\rm rad}^{\infty\ 1st} - M_{\rm IH}^{\infty}$	−0.000137	
	$M_{\rm rad}^{\infty\ 2nd} - M_{\rm IH}^{\infty}$	−0.000051	
Extrapolation error	$M_{\rm rad}^{\infty\ 1st} - M_{\rm rad}^{\infty\ 2nd}$	−0.000086	
Truncation error	$M_{\rm rad}^{\rm med\,1st} - M_{\rm rad}^{\infty\ 1st}$	0.000974	
	$M_{\rm rad}^{\rm med\,2nd} - M_{\rm rad}^{\infty\ 2nd}$	0.00130	
	$M_{\rm IH}^{\rm med} - M_{\rm IH}^{\infty}$	−0.000009	
$S_{\rm rad}{}^{\rm 1st}$	0.614951	15014.4	−3.3263
$S_{\rm rad}{}^{\rm 2nd}$	0.617925	24351.1	−3.37852
$S_{\rm IH}$	0.618414	−448868	−4.8117
Radiative v IH	$S_{\rm rad}^{\infty\ 1st} - S_{\rm IH}^{\infty}$	−0.003463	
	$S_{\rm rad}^{\infty\ 2nd} - S_{\rm IH}^{\infty}$	−0.000489	
Extrapolation error	$S_{\rm rad}^{\infty\ 1st} - S_{\rm rad}^{\infty\ 2nd}$	−0.002974	
Truncation error	$S_{\rm rad}^{\rm med\,1st} - S_{\rm rad}^{\infty\ 1st}$	0.00334	
	$S_{\rm rad}^{\rm med\,2nd} - S_{\rm rad}^{\infty\ 2nd}$	0.00426	
	$S_{\rm IH}^{\rm med} - S_{\rm IH}^{\infty}$	−0.000107	
$V_{\rm rec}^{\rm 1st}$	372.2	-1.6181×10^{9}	−4.28911
$V_{\rm rec}^{\rm 2nd}$	373.673	-7.54367×10^{8}	−4.00812
Truncation error	$V_{\rm rec}^{\rm 1st,\mathit{med}} - V_{\rm rec}^{\rm 1st,\infty}$	−4.273	
	$V_{\rm rec}^{\rm 2nd,\mathit{med}} - V_{\rm rec}^{\rm 2nd,\infty}$	−7.267	
Extrapolation error	$V_{\rm rec}^{\rm 1st,\infty} - V_{\rm rec}^{\rm 2nd,\infty}$	−1.473	

[a]This quantity is almost constant as a function of resolution.

TABLE IX. Same as Table VIII but for the B runs. Note that the final remnant dimensionless spin here is $\alpha_{\rm rem} = 0.68394 \pm 0.00005$, which is in close agreement (but outside the error bars) with the A case $\alpha_{\rm rem} = 0.68429 \pm 0.00010$.

Variable	X_∞	A	n
$M_{\rm rad}^{\rm 1st}$	0.961132	2187.04	−3.17927
$M_{\rm rad}^{\rm 2nd}$	0.961214	2077.94	−3.10559
$M_{\rm IH}$	0.961276	-8.05332×10^{12}	−9.22462[a]
Radiative v IH	$M_{\rm rad}^{\infty\ 1st} - M_{\rm IH}^{\infty}$	−0.000144	
	$M_{\rm rad}^{\infty\ 2nd} - M_{\rm IH}^{\infty}$	−0.000062	
Extrapolation error	$M_{\rm rad}^{\infty\ 1st} - M_{\rm rad}^{\infty\ 2nd}$	−0.000082	
Truncation error	$M_{\rm rad}^{\rm med\,1st} - M_{\rm rad}^{\infty\ 1st}$	0.000958	
	$M_{\rm rad}^{\rm med\,2nd} - M_{\rm rad}^{\infty\ 2nd}$	0.001278	
	$M_{\rm IH}^{\rm med} - M_{\rm IH}^{\infty}$	−0.00000259	
$S_{\rm rad}{}^{\rm 1st}$	0.629398	11168.2	−3.26154
$S_{\rm rad}{}^{\rm 2nd}$	0.632003	17393.8	−3.3056
$S_{\rm IH}$	0.631994	-1.91992×10^{10}	−7.27771
Radiative V IH	$S_{\rm rad}^{\infty\ 1st} - S_{\rm IH}^{\infty}$	−0.002596	
	$S_{\rm rad}^{\infty\ 2nd} - S_{\rm IH}^{\infty}$	0.000009	
Extrapolation error	$S_{\rm rad}^{\infty\ 1st} - S_{\rm rad}^{\infty\ 2nd}$	−0.002605	
Truncation error	$S_{\rm rad}^{\rm med\,1st} - S_{\rm rad}^{\infty\ 1st}$	0.003349	
	$S_{\rm rad}^{\rm med\,2nd} - S_{\rm rad}^{\infty\ 2nd}$	0.004258	
	$S_{\rm IH}^{\rm med} - S_{\rm IH}^{\infty}$	−0.0000531	
$V_{\rm rec}^{\rm 1st}$	370.09	-9.75205×10^{7}	−3.6121
$V_{\rm rec}^{\rm 2nd}$	373.311	-6.03304×10^{7}	−3.436760
Truncation error	$V_{\rm rec}^{\rm 1st,med} - V_{\rm rec}^{\rm 1st,\infty}$	−5.820	
	$V_{\rm rec}^{\rm 2nd,med} - V_{\rm rec}^{\rm 2nd,\infty}$	−8.073	
Extrapolation error	$V_{\rm rec}^{\rm 1st,\infty} - V_{\rm rec}^{\rm 2nd,\infty}$	−3.221	

[a]This quantity is almost constant as a function of resolution.

TABLE X. Table of RMS errors for third- and fourth-order fits for recoil, mass, and spin formulas.

	$V_{\rm rms,3rd}$	$V_{\rm rms,4th}$	$M_{\rm rms,3rd}$	$M_{\rm rms,4th}$	$\alpha_{\rm rms,3rd}$	$\alpha_{\rm rms,4th}$
RIT	5.52	2.55	0.00061	0.00021	0.00237	0.00072
SXS	14.47	20.01	0.00084	0.00036	0.00206	0.00047

TABLE XI. Table of third- and fourth-order fitting parameters for recoil, mass, and spin formulas.

	Third	Fourth		Third	Fourth		Third	Fourth
H	7137.601620	7367.250029	M0	0.952396	0.951507	L0	0.685797	0.686710
H2a	−1.781198	−1.626094	K1	−0.052082	−0.051379	L1	0.606328	0.613247
H2b	−0.801039	−0.578177	K2a	−0.000100	−0.004804	L2a	−0.135864	−0.145427
H3a	−0.644087	−0.717370	K2b	−0.090987	−0.054522	L2b	−0.123083	−0.115689
H3b	−1.116936	−2.244229	K2c	−0.002985	−0.000022	L2c	−0.005198	−0.005254
H3c	−0.880054	−1.221517	K2d	1.997610	1.995246	L2d	0.872193	0.801838
H3d	0.047189	−0.002325	K3a	−0.030344	0.007064	L3a	−0.047694	−0.073839
H3e	−0.966091	−1.064708	K3b	0.006774	−0.017599	L3b	0.023793	0.004759
H4a	0	−0.579599	K3c	−0.118419	−0.119175	L3c	−0.047273	−0.078377
H4b	0	−0.455986	K3d	0.044927	0.025000	L3d	1.751494	1.585809
H4c	0	0.010963	K4a	0	−0.068981	L4a	0	−0.003050
H4d	0	1.542924	K4b	0	−0.011383	L4b	0	−0.002968
H4e	0	−4.735367	K4c	0	−0.002284	L4c	0	0.004364
H4f	0	−0.284062	K4d	0	−0.165658	L4d	0	−0.047204
a	2.572817	2.611988	K4e	0	0.019403	L4e	0	−0.053099
b	1.528474	1.383778	K4f	0	2.980990	L4f	0	0.953458
c	0.657752	0.549758	K4g	0	0.020250	L4g	0	−0.067998
			K4h	0	−0.004091	L4h	0	0.001629
			K4i	0	0.078441	L4i	0	−0.066693

also note that, because the recoils from the A and B configurations did approach each other, effects due to finite initial separations are reasonably mitigated for separations of between $9M$ and $10M$ and above.

In conclusion we see that in order to have a robust measure of the recoil, we need to consider BHBs with sufficiently large initial separations and medium resolution, and we need to sum over modes up through $\ell = 6$.

In Fig. 24 we plot the radiated energy and the ratio of the final to initial mass derived from the radiated energy as a function of $1/r$ and $\ell_{\max}$. We see that the A and B configurations approach each other with an increase in resolution and larger observer radii. We also note that there are only small errors introduced by using $\ell_{\max}$ as small as $\ell = 4$. For the radiated angular momentum (see Fig. 25), the extrapolation error dominates, and while the A and B configuration results seems to converge to each other, the error bars are quite large. Again, we see that summing up through $\ell = 4$ is sufficient to obtain the final remnant spin.

To compute finite difference errors and consistency between the isolated horizons and radiation measures of the final remnant mass and spin, we perform a Richardson-like extrapolation of both the remnant mass and spin as calculated by both methods, as well as the recoil computed from the radiation, and fit to the form $X = X_\infty + A(1/h)^p$ where X_∞, A, and p are fitting parameters and X is the mass, spin, or recoil velocity. We show results in Table VIII and IX. Based on the results in the table, we estimate that the truncation errors in the final mass and spin, as measured by the highly accurate IH techniques, are $10^{-5}M$ for the mass and $10 - 4M^2$ for the spin, while the finite difference errors in the recoil are $\sim 8\ \mathrm{km\,s^{-1}}$.

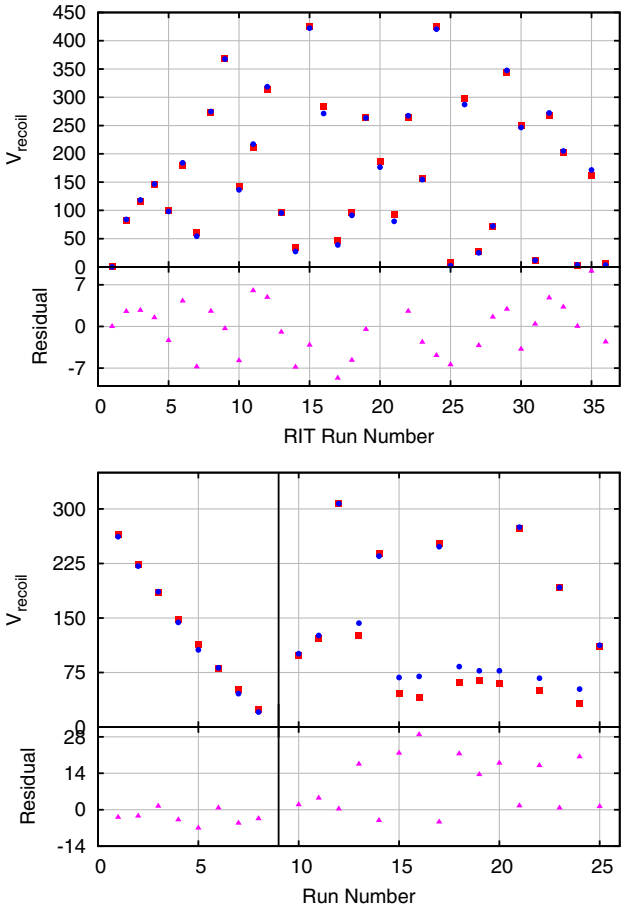

FIG. 26 (color online). Third-order recoil velocities and residuals for RIT runs (top panel) and AEI and SXS runs (bottom panel). Fits are given in red, and data in blue.

One final note, for the runs presented in the main body of the paper, we use extraction radii up to $r = 102.6M$, rather than $r = 190M$. We did this because we observed, at our working resolutions, a dissipation effect at larger radii in which the amplitude of $r\psi_4$ steadily decreases with radius in the outer zone.

We apply all these criteria to the rest of the new simulations that we perform in this paper to ensure similar error bars as the ones presented in this appendix. Note also that a similar, but independent, waveform-error analysis was carried out in Ref. [79].

APPENDIX B: THIRD-ORDER FITS

In this appendix we compare fits of the final remnant mass, spin, and recoil truncated at third order to our standard choice of fourth-order fits. We give the RMS errors in the third- and fourth-order fits in Table X and the fitting coefficients themselves in Table XI. Finally, we show the fits and residuals in Figs. 26–28.

We expect that the RMS errors in the third-order fits are larger than in the fourth-order fits. For the RIT recoil, this is the case (the RMS error more than doubles from 2.5 km s^{-1} to 5.5 km s^{-1}), but the RMS error in the SXS and AEI recoils actually decreases (20 km s^{-1} to 15 km s^{-1} and 6.8 km s^{-1} to 3.8 km s^{-1}, respectively).

The case is more clear for the fits to the final masses and spins where we included RIT data and SXS data, practically doubling the number of points (we also used the more accurate IH measures rather than measuring the radiated energy and angular momentum). Here we observe that for all data sets the RMS error increases by a factor of 3–5 when going from the fourth-order to third-order fits.

Finally, by comparing the fitting coefficients in the third- and fourth-order fits (see Table X), we get an estimate of the robustness of the fitting coefficients to the addition of still higher-order terms. This is important when using the fitting formulas to extrapolate to very high spins and very small mass ratios. Note that although some of the third- and fourth-order coefficients are quite different, the fitting curves themselves are very close to each other for moderate mass ratios ($1/10 \lesssim q \leq 1$) and spins ($0 \leq |\alpha_i| \lesssim 0.9$). However, we caution against using these formulas in regimes where the two predictions (third and fourth order) are substantially different.

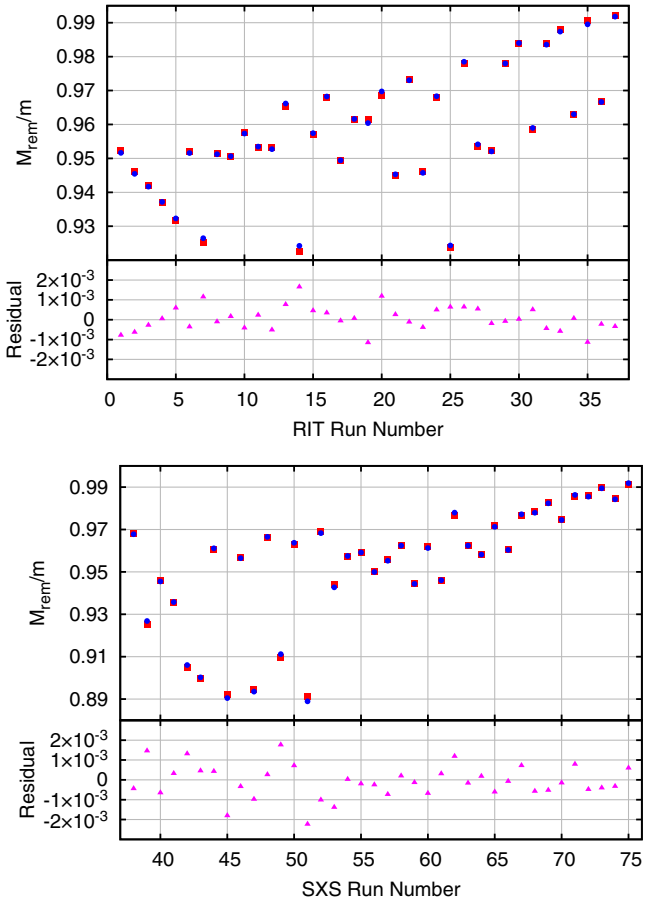

FIG. 27 (color online). Third-order remnant mass and residuals for RIT runs (top panel) and SXS runs (bottom panel). Fits are given in red, and data in blue.

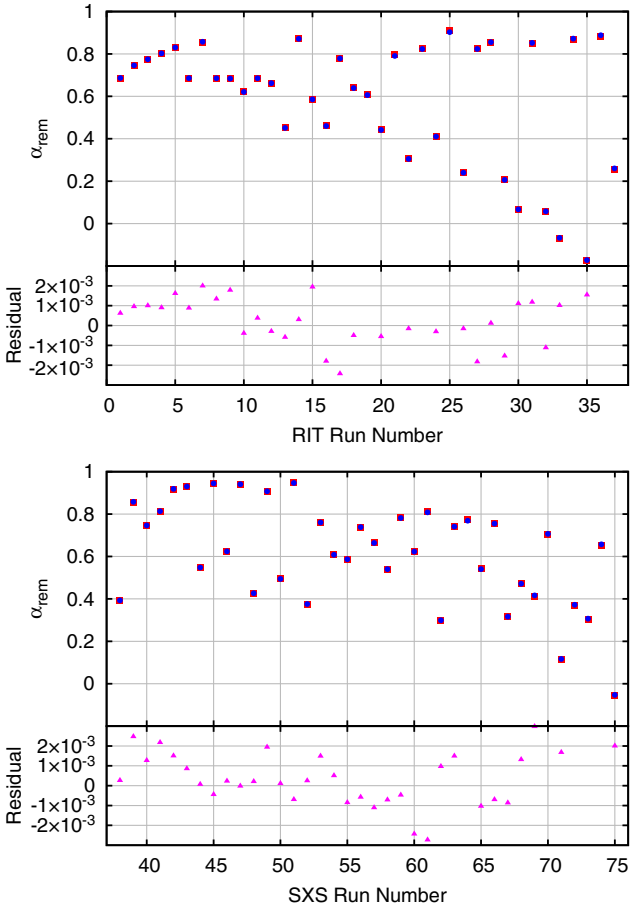

FIG. 28 (color online). Third-order remnant spin and residuals for RIT runs (top panel) and SXS runs (bottom panel). Fits are given in red, and data in blue.

[1] F. Pretorius, Phys. Rev. Lett. **95**, 121101 (2005).
[2] M. Campanelli, C. O. Lousto, P. Marronetti, and Y. Zlochower, Phys. Rev. Lett. **96**, 111101 (2006).
[3] J. G. Baker, J. Centrella, D.-I. Choi, M. Koppitz, and J. van Meter, Phys. Rev. Lett. **96**, 111102 (2006).
[4] M. Campanelli, C. O. Lousto, Y. Zlochower, and D. Merritt, Astrophys. J. **659**, L5 (2007).
[5] J. A. González, M. D. Hannam, U. Sperhake, B. Brugmann, and S. Husa, Phys. Rev. Lett. **98**, 231101 (2007).
[6] C. O. Lousto and Y. Zlochower, Phys. Rev. Lett. **107**, 231102 (2011).
[7] C. O. Lousto, Y. Zlochower, M. Dotti, and M. Volonteri, Phys. Rev. D **85**, 084015 (2012).
[8] C. O. Lousto and Y. Zlochower, Phys. Rev. D **87**, 084027 (2013).
[9] C. O. Lousto and Y. Zlochower, Phys. Rev. D **83**, 024003 (2011).
[10] Y. Zlochower, M. Campanelli, and C. O. Lousto, Classical Quantum Gravity **28**, 114015 (2011).
[11] C. O. Lousto, M. Campanelli, Y. Zlochower, and H. Nakano, Classical Quantum Gravity **27**, 114006 (2010).
[12] C. O. Lousto and Y. Zlochower, Phys. Rev. D **79**, 064018 (2009).
[13] S. C. Noble, B. C. Mundim, H. Nakano, J. H. Krolik, M. Campanelli, Y. Zlochower, and N. Yunes, Astrophys. J. **755**, 51 (2012).
[14] T. Bode, T. Bogdanovic, R. Haas, J. Healy, P. Laguna, and D. Shoemaker, Astrophys. J. **744**, 45 (2012).
[15] T. Bogdanovic, T. Bode, R. Haas, P. Laguna, and D. Shoemaker, Classical Quantum Gravity **28**, 094020 (2011).
[16] T. Bode, R. Haas, T. Bogdanovic, P. Laguna, and D. Shoemaker, Astrophys. J. **715**, 1117 (2010).
[17] R. Gold, V. Paschalidis, Z. B. Etienne, S. L. Shapiro, and H. P. Pfeiffer, Phys. Rev. D **89**, 064060 (2014).
[18] S. L. Shapiro, Phys. Rev. D **87**, 103009 (2013).
[19] B. D. Farris, R. Gold, V. Paschalidis, Z. B. Etienne, and S. L. Shapiro, Phys. Rev. Lett. **109**, 221102 (2012).
[20] B. D. Farris, Y. T. Liu, and S. L. Shapiro, Phys. Rev. D **84**, 024024 (2011).
[21] C. Palenzuela, L. Lehner, and S. L. Liebling, Science **329**, 927 (2010).
[22] C. Palenzuela, L. Lehner, and S. Yoshida, Phys. Rev. D **81**, 084007 (2010).
[23] M. Megevand, M. Anderson, J. Frank, E. W. Hirschmann, L. Lehner, S. Liebling, P. Motl, and D. Neilsen, Phys. Rev. D **80**, 024012 (2009).
[24] C. Palenzuela, M. Anderson, L. Lehner, S. L. Liebling, and D. Neilsen, Phys. Rev. Lett. **103**, 081101 (2009).
[25] T. Bogdanovic, C. S. Reynolds, and M. C. Miller, Astrophys. J. **661**, L147 (2007).
[26] M. Dotti, M. Volonteri, A. Perego, M. Colpi, M. Ruszkowski, and F. Haardt, Mon. Not. R. Astron. Soc. **402**, 682 (2010).
[27] M. Coleman Miller and J. H. Krolik, Astrophys. J. **774**, 43 (2013).
[28] G. Lodato and D. Gerosa, Mon. Not. R. Astron. Soc. **429**, L30 (2013).
[29] M. Dotti, M. Colpi, S. Pallini, A. Perego, and M. Volonteri, Astrophys. J. **762**, 68 (2013).
[30] A. Sesana, E. Barausse, M. Dotti, and E. M. Rossi, Astrophys. J. **794**, 104 (2014).
[31] S. Komossa, Adv. Astron. **2012**, 364973 (2012).
[32] D. Gerosa and A. Sesana, arXiv:1405.2072 [Mon. Not. Roy. Astron. Soc. (to be published)].
[33] J. D. Schnittman, Phys. Rev. D **70**, 124020 (2004).
[34] D. Gerosa, M. Kesden, E. Berti, R. O'Shaughnessy, and U. Sperhake, Phys. Rev. D **87**, 104028 (2013).
[35] J. A. González, U. Sperhake, B. Brugmann, M. Hannam, and S. Husa, Phys. Rev. Lett. **98**, 091101 (2007).
[36] F. Herrmann, I. Hinder, D. Shoemaker, P. Laguna, and R. A. Matzner, Astrophys. J. **661**, 430 (2007).
[37] M. Koppitz, D. Pollney, C. Reisswig, L. Rezzolla, J. Thornburg, P. Diener, and E. Schnetter, Phys. Rev. Lett. **99**, 041102 (2007).
[38] J. G. Baker, W. D. Boggs, J. Centrella, B. J. Kelly, S. T. McWilliams, M. C. Miller, and J. R. van Meter, Astrophys. J. **682**, L29 (2008).
[39] C. O. Lousto and Y. Zlochower, Phys. Rev. D **77**, 044028 (2008).
[40] L. E. Kidder, Phys. Rev. D **52**, 821 (1995).
[41] M. Campanelli, C. O. Lousto, and Y. Zlochower, Phys. Rev. D **74**, 041501(R) (2006).
[42] M. Campanelli, C. O. Lousto, Y. Zlochower, and D. Merritt, Phys. Rev. Lett. **98**, 231102 (2007).
[43] E. Racine, A. Buonanno, and L. E. Kidder, Phys. Rev. D **80**, 044010 (2009).
[44] M. Ansorg, B. Brügmann, and W. Tichy, Phys. Rev. D **70**, 064011 (2004).
[45] S. Brandt and B. Brügmann, Phys. Rev. Lett. **78**, 3606 (1997).
[46] Y. Zlochower, J. G. Baker, M. Campanelli, and C. O. Lousto, Phys. Rev. D **72**, 024021 (2005).
[47] P. Marronetti, W. Tichy, B. Brügmann, J. Gonzalez, and U. Sperhake, Phys. Rev. D **77**, 064010 (2008).
[48] C. O. Lousto and Y. Zlochower, Phys. Rev. D **77**, 024034 (2008).
[49] Cactus Computational Toolkit home page: http://cactuscode.org.
[50] Einstein Toolkit home page: http://einsteintoolkit.org.
[51] F. Loffler, J. Faber, E. Bentivegna, T. Bode, P. Diener *et al.*, Classical Quantum Gravity **29**, 115001 (2012).
[52] E. Schnetter, S. H. Hawley, and I. Hawke, Classical Quantum Gravity **21**, 1465 (2004).
[53] J. Thornburg, Classical Quantum Gravity **21**, 743 (2004).
[54] O. Dreyer, B. Krishnan, D. Shoemaker, and E. Schnetter, Phys. Rev. D **67**, 024018 (2003).
[55] M. Campanelli and C. O. Lousto, Phys. Rev. D **59**, 124022 (1999).
[56] J. Winicour, in *General Relativity and Gravitation*, Vol. 2, edited by A. Held (Plenum, New York, 1980), pp. 71–96.
[57] C. O. Lousto and Y. Zlochower, Phys. Rev. D **76**, 041502(R) (2007).
[58] We calculate eccentricities using the Newtonian formula $r^2\ddot{r} = me\cos\omega t$.
[59] C. O. Lousto and Y. Zlochower, Phys. Rev. D **89**, 104052 (2014).
[60] A. Ori and K. S. Thorne, Phys. Rev. D **62**, 124022 (2000).
[61] H. Nakano, M. Campanelli, C. O. Lousto, and Y. Zlochower, Classical Quantum Gravity **28**, 134005 (2011).
[62] C. M. Hirata, Phys. Rev. D **83**, 104024 (2011).

[63] M. van de Meent, Phys. Rev. D **90**, 044027 (2014).
[64] http://www.black-holes.org/waveforms.
[65] D. Pollney *et al.*, Phys. Rev. D **76**, 124002 (2007).
[66] T. Damour, Phys. Rev. D **64**, 124013 (2001).
[67] C. O. Lousto, H. Nakano, Y. Zlochower, and M. Campanelli, Phys. Rev. D **82**, 104057 (2010).
[68] H. Nakano, Y. Zlochower, C. O. Lousto, and M. Campanelli, Phys. Rev. D **84**, 124006 (2011).
[69] E. Barausse and L. Rezzolla, Astrophys. J. Lett. **704**, L40 (2009).
[70] E. Barausse, V. Morozova, and L. Rezzolla, Astrophys. J. **758**, 63 (2012).
[71] L. Rezzolla, R. P. Macedo, and J. L. Jaramillo, Phys. Rev. Lett. **104**, 221101 (2010).
[72] L. Rezzolla, P. Diener, E. N. Dorband, D. Pollney, C. Reisswig, E. Schnetter, and J. Seiler, Astrophys. J. **674**, L29 (2008).
[73] D. A. Hemberger, G. Lovelace, T. J. Loredo, L. E. Kidder, M. A. Scheel, B. Szilágyi, N. W. Taylor, and S. A. Teukolsky, Phys. Rev. D **88**, 064014 (2013).
[74] Q. Yu, Y. Lu, R. Mohayaee, and J. Colin, Astrophys. J. **738**, 92 (2011).
[75] K. R. Stewart, J. S. Bullock, E. J. Barton, and R. H. Wechsler, Astrophys. J. **702**, 1005 (2009).
[76] P. F. Hopkins, K. Bundy, D. Croton, L. Hernquist, D. Keres, S. Khochfar, K. Stewart, A. Wetzel, and J. D. Younger, Astrophys. J. **715**, 202 (2010).
[77] K. A. Sorathia, J. H. Krolik, and J. F. Hawley, Astrophys. J. **777**, 21 (2013).
[78] S. Privitera, S. R. P. Mohapatra, P. Ajith, K. Cannon, N. Fotopoulos, M. A. Frei, C. Hanna, A. J. Weinstein, and J. T. Whelan, Phys. Rev. D **89**, 024003 (2014).
[79] I. Hinder *et al.* (Perimeter Institute for Theoretical Physics), Classical Quantum Gravity **31**, 025012 (2014).